Determination and verification of the x-ray spectrum of a CT scanner

Ahmad Hassan,[a,c*] Martin Skalej[a] , Helmut Schlattl,[b] Christoph Hoeschen,[c]
[a]Otto von Guericke Universität Magdeburg, Universitätsklinikum Magdeburg A.ö.R., Institut für Neuroradiologie, Leipziger Str 44th, 39120 Magdeburg, Deutschland
[b] Helmholtz Zentrum München – German Research Center for Environmental Health, Institute of Radiation Protection, Ingolstädter Landstr. 1, 85764 Neuherberg, Deutschland
[c]Otto von Guericke Universität, Institut für Medizintechnik, Fakultät für Elektrotechnik und Informationstechnik Universitätsplatz 2, 39106 Magdeburg, Deutschland

Abstract. The accuracy of Monte Carlo (MC) simulations in estimating the computed tomography radiation dose is highly dependent on the proprietary x-ray source information. To address this, this study develops a new method to precisely estimate the x-ray spectrum and bowtie (BT) filter thickness of the x-ray source based on physical measurements and calculations. The static x-ray source of the CT localizer radiograph was assessed to measure the total filtration at the isocenter for the x-ray spectrum characterization and the BT profile (air-kerma values as a function of fan angle). With these values, the utilized BT filter in the localizer radiograph was assessed by integrating the measured air kerma in a full 360-degree cycle. The consistency observed between the integrated BT filter profiles and the directly measured profiles pointed to the similarity in the utilized BT filter in terms of thickness and material between the static and rotating x-ray geometries. Subsequently, the measured air kerma was used to calculate the BT filter thickness and was verified using MC simulations by comparing the calculated and measured air-kerma values, where a very good agreement was observed. This would allow a more accurate computed tomography simulation and facilitate the estimation of the dose delivered to the patients.

Keywords: CT localizer radiograph, multidetector CT, radiation dose, Monte Carlo simulations, x-ray spectrum, bowtie filter.

***First Author, E-mail: ahmad.hassan@ovgu.de,**

1 Introduction

The use of multidetector computed tomography (MDCT) has significantly increased the overall population’s exposure to radiation from computed tomography (CT) sources.[1-5] This increase is primarily due to patients’ relatively high radiation exposure during each examination, as well as the large number of examinations. To better understand the risks associated with MDCT examinations, scientists have attempted to calculate the radiation dose delivered to individual patients, both that delivered to each organ as well as the average collective dose.[6-15] These values are typically estimated using Monte Carlo (MC) software packages.[16] These packages require information about scanner geometry, in particular the focal spot to isocenter distance, fan angle, and z-axis collimation, which are all available in the scanner documentation.[17] It is crucial to obtain information about the energy spectra in order to accurately estimate the dose from a MDCT scan using MC simulation methods.[18] Understanding the energy spectra requires prior knowledge of the utilized filtrations that are acting collectively to harden the x-ray beam; however, information about design, shape, and composition of the implemented filtrations is proprietary. This limits the accessibility of such information to researchers, and thereby impedes their ability to accurately model the x-ray spectra of a given scanner.

Different approaches have been used to investigate the proprietary aspect of scanner-specific source information, specifically the x-ray spectra and bowtie (BT) filter thickness, for both static and rotating x-ray sources.[19-26] For static x-ray sources, Turner et al. describe a method for estimating x-ray spectra based on physical measurements of the half-value layer (HVL).[19] In the same study, the static x-ray source was used to estimate the BT filter profile by measuring air kerma as a function of the fan angle, thus determining an equivalent filter. This method can be used to estimate the number of photons in the off-centerline spectra; however, using this method it is not possible to match the relative number of photons with the spectral shape since only one material thickness (aluminum) is varied.

For rotating sources, Boone et al proposed a method utilizing a dosimeter placed at the edge of an x-ray field generated by a rotating source.[20] They then used the air-kerma rate to determine the angle-dependent BT filter attenuation. Theoretically, this method effectively characterizes the BT filter used in commercial CT scanners. There are some limitations, however, including the need for real-time dosimeter readings with sufficient sensitivity and high temporal resolution. Another challenge is the inability to determine the HVL of a rotating x-ray source when characterizing the x-ray spectrum. These limitations were overcome in subsequent studies.[21-24] In addition, a novel method was later proposed that allowed for an angle-dependent estimation of the x-ray spectrum for rotating sources.[25] This technique was experimentally tested using a CT scanner, and the results compared with the data provided by the manufacturer. The results demonstrate that the measurement of the incident spectrum over a wide range of angular trajectories is possible with both a high level of accuracy and stability. In addition, Yang et al proposed a new method to measure CT filter profiles using a linear array solid-state detector for rotating x-ray sources.[26] This approach utilizes both accurate geometric calibration and high angular resolution.

In previous studies, the estimated thickness of the BT filter was based on physical measurements of static or rotating x-ray sources.[19-32] In this study, static x-ray sources are directly involved in the estimation of the BT filter thickness, while rotating x-ray sources are indirectly involved. The characterization of the BT attenuation profile across the fan angle of the x-ray source necessitates the use of the static x-ray source of the CT localizer radiograph. The same measurements are performed using the rotating x-ray source of the clinical protocols. The resulting profiles of the BT filter are qualitatively compared with the BT profiles from the static x-ray source. This study introduces a new theoretical method for making such a comparison possible. This method involves mathematically integrating the measured profile of the static x-ray source across all incident angles in a full 360-degree cycle. The integrated BT filter profile is then compared with the measured BT profile of the rotating x-ray source of the clinical protocols. These results could provide a depiction of the BT filter utilized for both rotating and static x-ray sources.

In this paper, physical measurements made using the CT scanner are presented along with the calculations necessary to calculate the BT filter thickness. The accuracy of the resulting BT filter thickness is then assessed by comparing the results of MC simulations with physical measurements of static x-ray sources. Similarly, the results of experimental measurements for rotating sources are compared with the simulated MC simulations of multiple CT dose index (CTDI) phantoms.

2 Materials and Methods

2.1 CT scanner model

All measurements were performed using a SOMATOM Definition 64 CT scanner (Siemens Medical Solutions, Forchheim, Germany).[33] The x-ray tube anode angle was 7°. The distance from the focal spot to the isocenter (SID) and the detector (SDD) was 595 mm and 1085 mm respectively. The scanner operated in both axial and helical modes at tube voltages of 80 kV, 100 kV, 120 kV, and 140 kV. Two different focal spots were used, with dimensions of 0.7×0.7 mm^2 and 0.9×1.1 mm^2 corresponding to small and large focal spots respectively. The system operated at different x-ray beam collimations, given in the $N \times T$ format where N represents the number of data channels and T represents the nominal width of each data channel. For this study, x-ray collimation of 3.6 mm and 38.4 mm were used for static and rotating x-ray sources respectively.

2.2 Ionization chamber

An ionization chamber type 30009 connected to a Unidos electrometer (PTW, Freiburg, Germany) was used to measure the physical air kerma. The nominal active volume of the ionization chamber was 3.14 cm^3 with a sensitive measuring length of 10 cm and an outer diameter of 0.9 cm. The homogeneity of the detector response was less than ± 5 % for (70 -150) kV.[34]

2.3 Nomex multimeter

The Nomex multimeter is a noninvasive device that consists of electronics and multiple channels of silicon semiconductor detector according to IEC 61674.[35] The system was approved by the German law as a diagnostic dosimeter by the German National Metrology Institute, PTB.[36] The Nomex device was calibrated for many different imaging modalities, including radiography, fluoroscopy, mammography (Mo/Mo, Mo/Rh, W/Al, W/Rh, W/Ag, Rh/Rh), and computed tomography.[37] The Nomex multimeter was designed for the purpose of measuring different quantities during one single radiation exposure, including air kerma, air-kerma rate, tube voltage, and total filtration.

In this study, we use the Nomex multimeter to measure the total filtration for the following tube voltages: 80 kV, 100 kV, 120 kV and 140 kV. The essential parts of the Nomex multimeter system are illustrated in Figure 1. Parts #1 and #2 represent the multi-channel detector and the electronic areas respectively. Part #3 represents the location of the central axis of the source. Part #4 (the shaded grey area) is illustrated by the 1 mm width bar that identifies the center of the 3 mm wide measurement area. This measurement area indicates the active detector zone for the measurements of total filtration of the CT scan. The measurement area shown in grey must be fully irradiated. The measurements of the estimated total filtration area have an accuracy of ± 10%, or 0.5 mm.[38] Part #5 indicates the status of the device: for example, a green led light indicates that the device is ready for use.

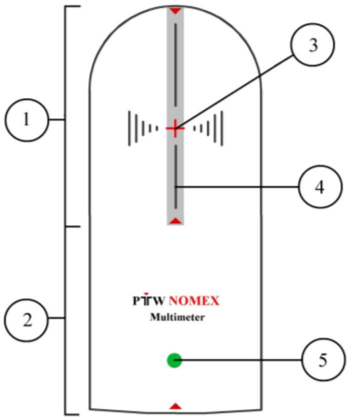

Fig. 1 The Nomex multimeter active area in the measurement of the total filtration for CT scan.

2.4 Physical measurements

2.4.1 Static x-ray source measurements

Most MDCT scanners have more than one BT filter. These BT filters are dependent on the tube voltage, and more importantly, on the selected field of view (FOV). A large field of view (LFOV) requires a correspondingly wide filter to cover the entire fan beam when scanning the patient. Likewise, clinical protocols for small FOVs (SFOVs) call for a small BT filter due to the reduced diameter of the scanned area. For this study, CT localizer radiographs of child neck protocols and adult abdomen protocols were selected to represent SFOVs and LFOVs respectively. The static x-ray source was positioned at the 90°, and the patient's table was adjusted such that it was outside the measuring field. Air kerma was measured across the fan angles with a plastic ruler. The ruler dimensions were 780 mm, 60 mm, and 8 mm in x, y and z-axes respectively.

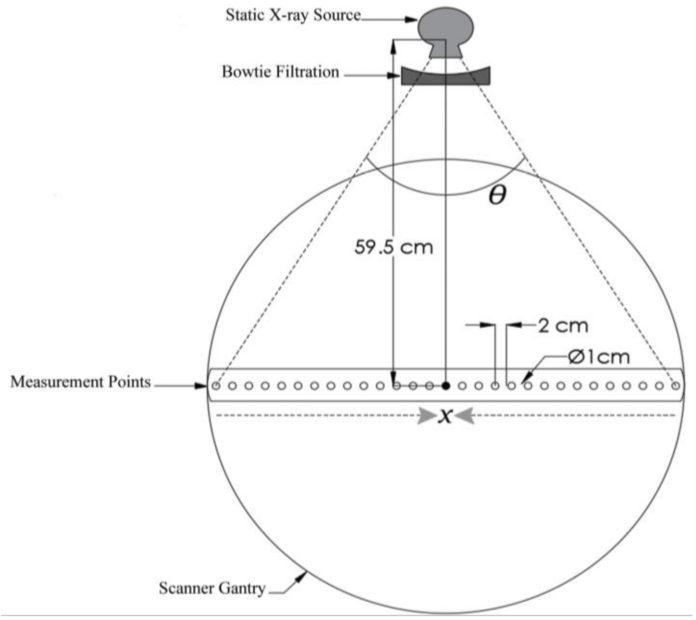

Fig. 2 Schematic view of BT profile measurements across the fan angle of the static x-ray source.

A lathe was then used to drill 29, 1 cm diameter holes in a row, spaced 2 cm from isocenter to isocenter. The tolerance for all dimensions in the manufactured ruler was ± 0.1 mm. The ruler was placed across the opening of the CT gantry, and the ionization chamber was placed in the opening holes within the center of the collimation along the z-axis of the scanner, as illustrated in Fig. 2. Measurements were taken for tube voltages of 80, 100, 120 and 140 kV, while keeping the default settings for the other parameters constant. The parameters of the experiments were the following: tube current of 300 mA, collimation width of 3.6 mm, and exposure time of 2.7 s and 5.3 s for SFOV and LFOV CT localizer radiographs respectively.

2.4.2 Half value layer measurements.

The half value layer (HVL) measurements were measured for tube voltages of 80 kV, 100 kV, 120 kV, and 140 kV. The static x-ray source of the CT localizer was placed at the 90° position because the x-ray source cannot be placed at the standard position (180°) when collecting HVL measurements, as shown in Figure 3. The ionization chamber was placed at the isocenter hole of the plastic ruler in the direction of the central ray. The default settings used in the static x-ray source experiments (section *2.4.1*) were also used in the HVL experiments for both SFOV and LFOV CT localizer radiographs. The HVL was estimated by increasing the thickness of the aluminum layers until the air kerma was equal to one half of the measured air kerma free-in-air without aluminum layers.

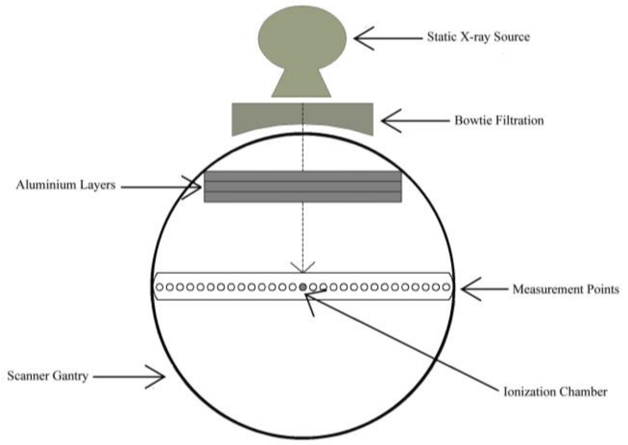

Fig. 3 Experimental set up of HVL measurements.

2.4.3 Rotating x-ray source measurements

The attenuation of the BT profile was measured as a function of fan angle for the rotating x-ray source. These physical measurements were obtained for the purpose of comparison only. The ruler was positioned across the CT gantry, and the ionization chamber was placed in the opening holes within the center of the collimation along the z-axis of the scanner, as illustrated in Fig. 4. Two different clinical protocols were selected to represent SFOV and LFOV, and the rotating source in both protocols was operated in the helical mode. For SFOV, the child neck and abdomen protocols were selected using default settings of 90 mA tube current and 38.4 mm collimation width. The scan times were 7 s for the child neck protocol and 1 s for the child abdomen protocol. For LFOV, the clinical protocols of the adult abdomen and thorax were used with settings of 4 s scan time, 38.4 mm collimation width, and with tube currents of 210 mA and 110 mA for abdomen and thorax protocols respectively. Notably, all measurements were obtained at a tube voltage of 120 kV, which is commonly used in clinical protocols.

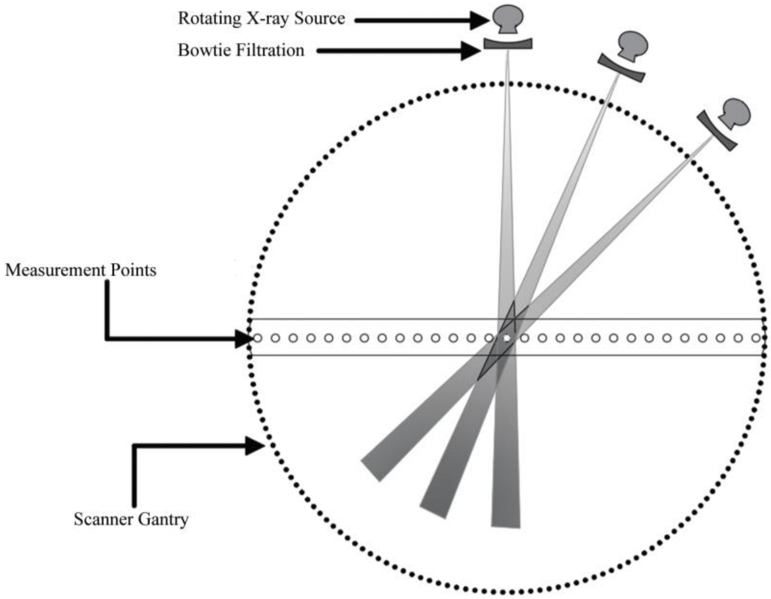

Fig. 4 Experimental scheme of BT profile measurements of attenuation of the rotating x-ray source of the clinical protocols.

2.5 Integration of the static x-ray source measurements

Several BT filters are used in MDCT studies today. The selection of a particular BT filter depends on the tube voltage, and more importantly, the FOV. The same BT filter can be used in different operational modes of the x-ray source. In order to evaluate this, a direct comparison can be made between the BT filter profiles experimentally measured as a function of angle for both static and rotating x-ray sources. However, the different status of the static and rotating x-ray sources made such a direct comparison invalid. In this study, a new method (hereafter referred to as the integration method) is proposed to make the measurements of static and rotating sources comparable. The method utilizes an integrated x-ray source, resulting from the integration of static x-ray source measurements across a 360-degree cycle. The resulting estimate of the BT profiles from the integration of static x-ray source measurement values was then compared to the directly measured BT profiles of the actual rotating x-ray source of the clinical protocols. This provided useful information about the consistency or discrepancy of the BT filters used for static and rotating x-ray sources. This could eliminate the necessity of relying on physical measurements of the rotating x-ray source to calculate the BT filter thickness of a given scanner.

Figure 5 illustrates the relationship between the integrated static x-ray source and the static x-ray source used in this experiment. For the integrated static source, the origin of the coordinate system is placed at the isocenter (x_0). We define (S_α) as the point at which the source makes an angle (α) with the positive x-axis. Using this terminology, the static case can be viewed as a unique configuration of the integrated static case ($when\ \alpha = \frac{\pi}{2}$); hence, the position of the static source can be described by the coordinates (0, R). This case is denoted by(S), where $S = S_{\frac{\pi}{2}}$.

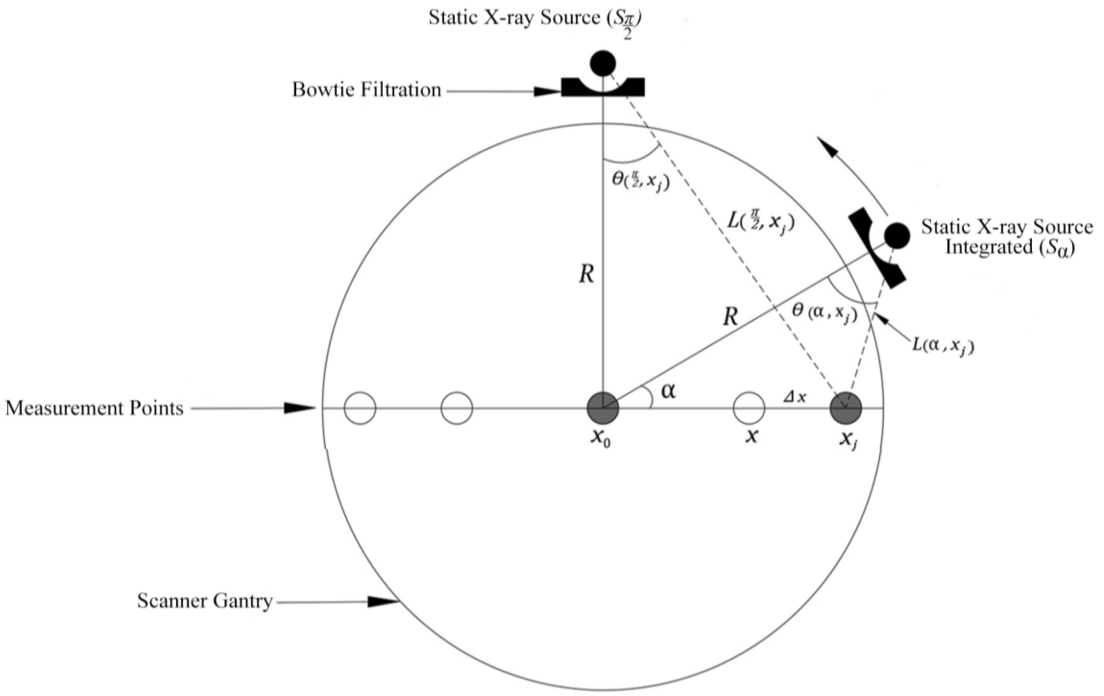

Fig. 5 Schematic view of the geometrical relationship between a static x-ray source and the integrated static x-ray source resulting from the integration method.

The experimental measurements of the static x-ray source can help determine whether the attenuation profile of the BT filter can be inferred from the integration of the static x-ray source values. The measurement procedures are explained in Section *2.4.1*, and Fig. 2 shows a detailed schematic of the experimental geometry and set-up. The static x-ray source was positioned at $\frac{\pi}{2}$, and the ionization chamber was placed in the opening holes of the ruler laid across the x-axis so that the active length of the ionization chamber was centered along the z-axis of the scanner.

The ionization chamber was shifted across the measurement points to the isocenter ($x_0 := 0$) by a distance of

$$x_j = j\Delta x \tag{1}$$

where j = -14,..0,..14 (the number of measurement points placed across x-axis= 29) and Δx = 2 cm.

For static sources, the distance from the x-ray source to the measurement points $L\left(\frac{\pi}{2}, x_j\right)$ is given by

$$L\left(\frac{\pi}{2}, x_j\right) = \sqrt{R^2 + x_j^2} = \sqrt{R^2 + (j\Delta x)^2}\,. \tag{2}$$

For the integrated static sources, S_α, the distance between the x-ray source and a measurement point x_j , is defined by $L\left(\alpha, x_j\right)$

$$L\left(\alpha, x_j\right) = \sqrt{x_j^2 + R^2 - 2\mathrm{R}x_j \cos\alpha} \tag{3}$$

The angle $\theta(\alpha, x_j)$ is defined as the fan angle between the x-ray source and the measurement points relative to the central ray. For static sources, this angle can be calculated using the following equation:

$$\theta\left(\frac{\pi}{2}, x_j\right) = \arctan\left(\frac{j\Delta x}{\mathrm{R}}\right) \tag{4}$$

For the integrated static sources, the angle can be calculated by the following equation:

$$\theta\left(\alpha, x_j\right) = \arcsin\left(\frac{x_j sin\alpha}{\left(\alpha, x_j\right)}\right) \tag{5}$$

The air kerma-length-product for any of the measurement points across the x-axis is a function of the distance from, and the angles to, the source. The air kerma-length-product at the point x_j is denoted by $KL\ (\alpha, x_j)$ for the integrated static source S_α, and thus $KL\ (\frac{\pi}{2}, x_j)$ denotes the air kerma at the point x_j for the static source S. At the isocenter point x_0, KL is the same for both the static and integrated static cases for any angle α. This can be written by:

$$KL(\frac{\pi}{2}, x_0) = KL(\alpha, x_0) = KL_{isocenter} \tag{6}$$

At each of the measurement points, the relative air-kerma length product for the BT filter across the fan beam is computed by:

$$KL\left(\frac{\pi}{2}, x_0\right) = \ KL(\alpha, x_0) = KL\big(\alpha, x_j\big)\frac{L(\alpha, x_j)}{R} \tag{7}$$

This formula is valid as long as the field length remains smaller than the length of the employed pencil ionization chamber (10 cm). In this case, the measurement field length *S* is proportional to the distance *L*. Thus,

$$K \sim \frac{1}{L^2} \text{ and } S \sim L,$$

so that

$$KL \sim \frac{1}{L} \tag{8}$$

where *K* = air kerma

The total air-kerma length product at the point x_j of the integrated static x-ray source is denoted by $KL(x_j)$. This KL profile at each measurement point is calculated from the static source profile. This is done by integrating the x-ray at all beam angles of the integrated static source, taking into account the distance between the source and the measurement points. In this case, the total air-kerma length product of the integrated static source having completed a full 360-degree cycle is calculated by:

$$KL(x_j) = \int_0^{2\pi} KL\left(\alpha, x_j\right) \, d\alpha = \int_0^{2\pi} \frac{KL_{isocenter}\, R}{L(\alpha, x_j)} \, d\alpha \tag{9}$$

In summary, x-ray incidents from the integration of the static source were computed for every measurement point along the horizontal *x*-axis for all possible beam angles using the air-kerma length product values from a static x-ray source profile. The resulting air-kerma-length-product values from the integration were then compared with the measured air-kerma-length-product values obtained from the rotating x-ray source of the clinical protocols (section *2.4.3*).

2.6 X-ray spectrum

The x-ray spectrum of the tube energy was characterized by measuring the total filtration using a Nomex multimeter (PTW, Freiburg, Germany) positioned at the central beam axis of the isocenter of the scanner with an x-ray source static at the 90° position. CT localizer radiographs of the SFOV and LFOV with default settings (section *2.4.1*) were independently used to measure the TF thickness for tube voltages of 80 kV, 100 kV, 120 kV, and 140 kV. The SpekCalc program[39] was then used to generate x-ray spectra based on the measured TF thickness (Al–equivalent) for both the SFOV and LFOV at each voltage.

Validation of the Nomex multimeter output (TF thickness) for SFOV and LFOV was performed using the measured HVL values at all energy levels between 80 kV and 140 kV for both SFOV and LFOV (section *2.4.2*). Using the SpekCalc program, x-ray spectra were generated for an anode angle of 7°, while the aluminum thickness (mm) was increased until the HVL value equaled that of the experimentally measured HVL value.

2.7 Bowtie filter calculation

The primary focus of this study was to provide an estimation of the BT filter thickness that matched as closely as possible the actual BT filter thickness present in the specific CT scanner used. In this section, the algorithm used to provide the BT filter thickness as a function of fan angle is further explained. The required inputs were 1) the measured air-kerma values at each of the measurement points of the CT localizer radiographs, and 2) the x-ray spectra calculated using the measured TF thickness of each kVp. The calculation of the BT filter thickness was done separately using the experimental measurements taken for SFOV and LFOV.

Air kerma of the static x-ray source was measured for a set of points on the path of the x-ray beam. If the BT filter was placed in the path of the x-ray source, the BT filter thickness would need to be known to produce meaningful measurement values. To achieve this, the initial values of the BT filter thickness in a specified range were set for each of the test points. The range was necessary to allow adjustments in the filter thickness. For each of the points, the attenuation of the x-ray spectrum was calculated for the filter thickness (and angle) through which it passed. This approach takes into account the geometry of the experiment, specifically the distance from the source to the isocenter, the distance between each measurement point, and the distance from the measurement point to the isocenter. It also accounts for both the perpendicular and the off-perpendicular aspect of the beam's transmission through the filter. Usually a beam will travel a greater distance through the same thickness of the filter material if travelling non-perpendicularly to the filter's surface, as opposed to perpendicularly to the surface. After simulating the filter attenuation of the x-ray spectrum, the resulting transmitted radiation through the filter at each of the test points was obtained by assuming an exponential attenuation profile. Consequently, the calculated air kerma was compared with the measured air kerma at each test point. Where the calculated air kerma was greater than the measured kerma value, the filter thickness was increased at that point. Similarly, when the calculated air kerma was less than the measured kerma value, the filter thickness was decreased at that point. After updating the values and ranges of filter thickness at all test points, a chi-squared test was performed. In this case, the calculated air kerma corresponding most closely to the measured air kerma was found when x^2 was minimized:

$$x^2 = \frac{(K_{calc} - K_{meas})^2}{K_{calc}} \tag{13}$$

The following are the sequential steps of calculating the BT thickness.

- Simulating the filter attenuation.
- Calculating the air kerma.
- Adjusting the BT filter thickness.
- Reducing the range of the BT filter thickness and calculating the chi-square statistic.
- Iteratively repeating this step until a minimum value of x^2 is achieved.
- Accepting the BT thickness profile corresponding to the x^2 minimum as the BT filter shape.

This method was implemented by using routines coded in the computer language C. The result was a complete set of equivalent BT filter thicknesses based on each of the generated x-ray spectra. It is worth mentioning that the main BT filter material was presumed to be Teflon (PTFE).[20,21,40]

2.8 Physical measurement of the CTDI phantoms

Measurements were performed on the standard CTDI body (320 mm in diameter), CTDI head (160 mm in diameter), and CTDI child (100 mm in diameter) phantoms. These phantoms are 150 mm in length and made of polymethylmethacrylate (PMMA) material. The phantoms have 5 holes into which a PMMA rod or the ionization chamber is inserted. All of the scans were performed using the helical mode, in which the scan length covers the entire phantom. The child neck clinical protocol for the SFOV was used with scan settings of 90 mA tube current, 5 s scan time, 0.6 pitch, and 38.4 mm beam collimation. The adult thorax clinical protocol for the LFOV was used with scan settings of 110 mA tube current, 0.6 pitch, 2 s scan time and 38.4 mm beam collimation. Air kerma was measured at all available tube voltages, 80, 100, 120 and 140 kV, by inserting the ionization chamber into each of these phantoms at the center hole and also at the four periphery holes (Right, Left, Top, Bottom).

2.9 Overview of the Monte Carlo method

2.9.1 Monte Carlo simulations

The experimental measurements were verified using the EGSnrc MC particle transport code (version V4-2-3-0).[41] EGSnrc tracks particles across all energies corresponding to those used in the experiments. For the purpose of this study, photons were simulated with a low-energy cutoff of 2keV. The remaining particle kinetic energy was deposited locally. The radiation interaction processes considered were photoelectric absorption and Rayleigh scattering. The material cross-sections for photoelectric absorption and Rayleigh scattering are consistent with the values in the XCOM/NIST database. The EGSnrc simulation also took into account the bound Compton scattering and the photo-electrons from the K, L, and M valence shells.

2.9.2 Modeling of the CT source

The source subroutine of the EGSnrc simulation code was written so that different settings of the CT scanner could be modeled using user-definable input parameters, including geometric factors, x-ray spectra, modes of acquisition, and BT filtration thickness. Geometric factors selected for each simulation included the dimensions of the x-ray source with respect to the simulated object in the x, y, and z-axes, SID, focal spot size, and beam collimation along the z-axis. This information was obtained from the documentation supplied with the CT scanner (section *2.4.1*).

The x-ray source model assumes the photons are emitted from a location within the x-ray tube anode. The x-ray spectra generated by the SpekCalc program based on the measured TF thickness for each tube voltage were used to simulate the x-ray spectra for the CT scanner (section *2.6*).

Different modes of acquisition were implemented in the EGSnrc code, including axial, helical (with the ability to input desired pitch), and static beam position (with the ability to select the angle at which the beam is parked). In this study, the static and contiguous axial scans were simulated corresponding to the measurements made using the CT scanner.

The Teflon BT filter thickness was simulated based on a polynomial shape resulting from fitting the rational function to the calculated thickness across all measurement points. The radiation transport process through the filter was simulated by reducing the statistical weight of each incident photon according to its attenuation by the filter. Thus, scatter radiation emitted by the filter was ignored. This has been proven to be justified in a side computation.

2.9.3 Simulation of the experimental objects

The plastic ruler used in the experiment was simulated to accurately represent the measurement points on the static x-ray source. The geometric dimensions and position of the ruler were simulated as explained in section *2.4.1*. The ruler was discretized into segments, where the total number of voxels were 1560, 120, and 4 in the x, y, and z directions respectively. The voxel dimensions were 0.5 mm *0.5 mm * 2 mm for the x, y, and z-axes respectively. The voxel material was PMMA. The holes were modeled in a small circular pattern with a diameter of 10 mm into which air kerma was determined.

The standard CTDI phantoms (body, head, and child) were simulated in order to verify the physical measurements of the rotating x-ray source. A Cartesian coordinate system was defined using the model dimensions so that the isocenter of the modeled phantoms coincided with the isocenter of the scanner, the z-axis was collinear with the axis of the scanner, and the x-y plane was coplanar with the CT slice plane. The computational models had non-isotropic voxels and were described as set of slices, where each slice consisted of a number of voxels. The number of voxels in the x, y, and z-axes were 640, 640, and 6 for the CTDI body, 320, 320, and 6 for the CTDI head, and 200, 200, and 6 for the CTDI child. The voxel dimensions for all computational models were 0.5 mm, 0.5 mm, and 25 mm in x, y, and z-axes respectively. Within the designated volume, voxels were defined to contain PMMA material and have air present around the simulated voxels. In the central 4 slices, five 9 mm diameter, cylindrical holes were inserted. In these holes dose values were recorded to provide air kerma. The CT scanner table was approximated as a 10 mm thick rectangular carbon slab and modeled with each phantom.

After the experimental measurements were recorded for the static and rotating x-ray sources, the source subroutine was used to simulate all measurement configurations for each experiment based on the parameters for the geometric factors, the x-ray spectra, the modes of acquisition, the BT filter profile, and the simulated object. In each simulation, 100 million photon histories were pursued, resulting in a statistical uncertainty of less than 1%. This number of histories was chosen to achieve a compromise between the relative error and reasonable computational times.

3 Results

3.1 SFOV integration

Figures 6(a) and 6(b) depict normalized attenuation profiles of the BT filter measurements for a rotating x-ray source, and the measurements from a static x-ray source integrated in a complete 360-degree cycle at 120 kV for child neck and child abdomen protocols respectively. A strong correspondence was observed between the integrated static source and the rotating source for SFOV at all measurement points. The Root Mean Square Error (RMSE) was 0.83 % for the child neck protocol and 1.11 % for the abdomen protocol.

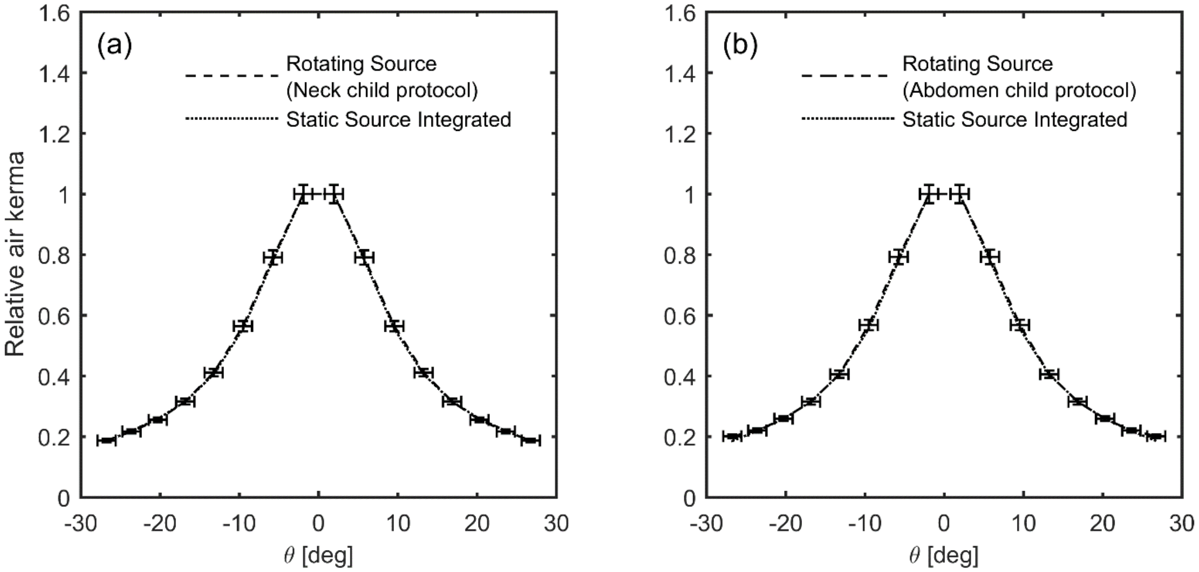

Fig. 6 Comparison of normalized profiles of BT filter from the integrated air kerma and the measured air kerma for the SFOV at 120 kV. (a) Static source integrated and child neck protocol. (b) Static source integrated and child abdomen protocol.

3.2 LFOV integration

The results of the comparison between the attenuation profile of the BT filter measurements from a rotating source and the integrated measurements from a static x-ray source are shown in Figures 7(a) and 7(b). The measurement and integration data sets were each normalized to the peak value at the isocenter (0 degree). A strong correlation between the integrated static source and the rotating source was noted in adult protocols for LFOV. In this case, the RMSE was 1.83 % for the thorax protocol and 2.09 % for the abdomen protocol.

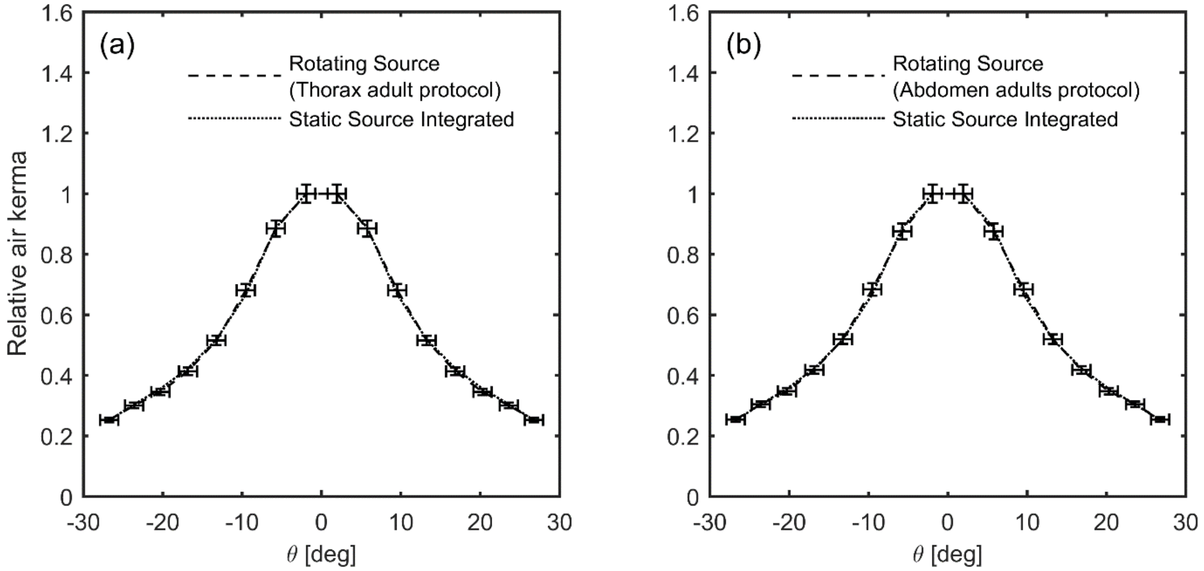

Fig. 7 Comparison of normalized profiles of BT filter from the integrated air kerma and the measured air kerma for the LFOV at 120 kV. (a) Static source integrated and adult thorax protocol. (b) Static source integrated and adult abdomen protocol.

3.3 X-ray spectrum

The results of the measured HVL described in section *2.4.2* are presented in Table 1 and Table 2, for SFOV and LFOV respectively, for all energy levels between 80 kV and 140 kV. These tables also include the results of the measured TF thickness values from the Nomex multimeter and the TF thickness values from the SpekCalc program for SFOV and LFOV at each of the available beam energies. A strong correlation was noted between the measured TF thicknesses from the Nomex multimeter device and the estimated TF thicknesses from the SpekCalc program, resulting from matching the HVL measurements for both SFOV and LFOV. The maximum percentage difference was 2.53 % at 80 kV for SFOV, and 1.68 % at 80 kV for LFOV. The percentage difference at each energy level was within the accuracy limit of ± 10% for the TF estimation of the Nomex multimeter device (section *2.3*).

Table 1. Measured TF thickness in mm Al from the Nomex multimeter device and the resulting TF thickness in mm Al from the SpekCalc program, resulting from matching the measured HVL in mm Al for all tube voltages ranging from 80 kV to 140 kV for SFOV.

Energy level	Measured HVL (mm)	Measured TF from Nomex multimeter (mm)	TF from the SpekCalc program (mm)	Percentage difference (%)
80	6.07± 0.1 mm	12 ± 0.5 mm	11.70	2.53
100	7.40± 0.1 mm	12 ± 0.5 mm	11.75	2.10
120	8.50± 0.1 mm	12 ± 0.5 mm	11.95	0.42
140	9.40± 0.1 mm	12 ± 0.5 mm	11.95	0.42

Table 2. Measured TF thickness in mm Al from the Nomex multimeter device and the resulting TF thickness in mm Al from the SpekCalc program, resulting from matching the measured HVL in mm Al for all tube voltages ranging from 80 kV to 140 kV for LFOV.

Energy level	Measured HVL (mm)	Measured TF from Nomex multimeter (mm)	TF from the SpekCalc program (mm)	Percentage difference (%)
80	6.10± 0.1 mm	12 ± 0.5 mm	11.80	1.68
100	7.45± 0.1 mm	12 ± 0.5 mm	11.95	0.42
120	8.52± 0.1 mm	12 ± 0.5 mm	12.05	0.42
140	9.45± 0.1 mm	12 ± 0.5 mm	12.18	1.49

3.4 Bowtie filter calculation

3.4.1 Bowtie filter thickness for SFOV

Figure 8 depicts derived BT filter thicknesses for SFOVs. The filters are made of aluminum and Teflon, and the measurements are based on SFOVs for beam energies of 80 kV to 140 kV. The maximum calculated BT filter thickness observed at the periphery was 8.57 cm, and the maximum measured TF thickness at the center was 1.2 cm for all energy levels between 80 kV and 140 kV. BT filters of equal thickness from the two materials showed strong correlations at each energy level. The maximum variation across all calculated BT thicknesses was 8.66% for all tube voltages, with a slight deviation in the BT filter thickness at 140 kV.

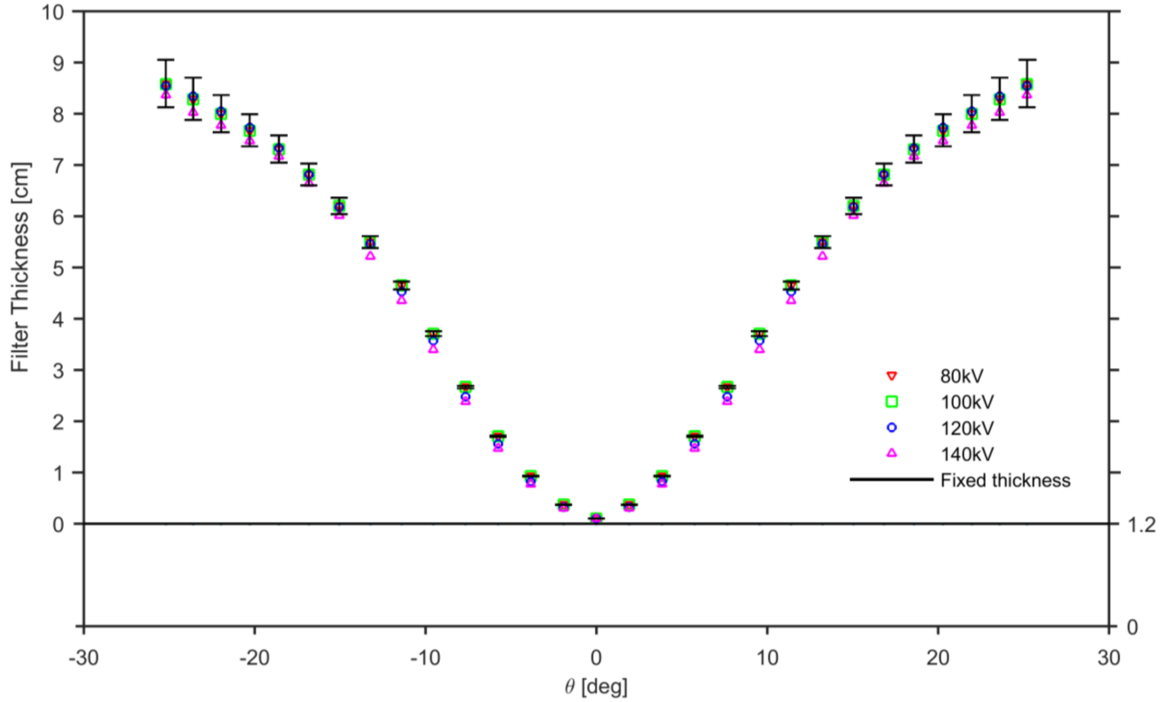

Fig. 8 Calculated BT filter thickness for SFOV at energy levels of 80 kV, 100 kV, 120 kV, and 140 kV. The measured BT filter thickness is shown for aluminum filters (horizontal black line) and Teflon filters (colored lines).

3.4.2 Bowtie filter thickness for LFOV

The resulting estimates of BT filter thickness for all tube voltages from 80 kV to 140 kV are presented in Figure (9) for LFOV. The BT filter thickness at the periphery was 6.05 cm, and the TF thickness at the center was 1.2 cm. A strong correlation was found among the calculated BT thicknesses across all fan angles, with a maximum variation of 4.90 % for all tube voltages ranging from 80 kV to 140 kV.

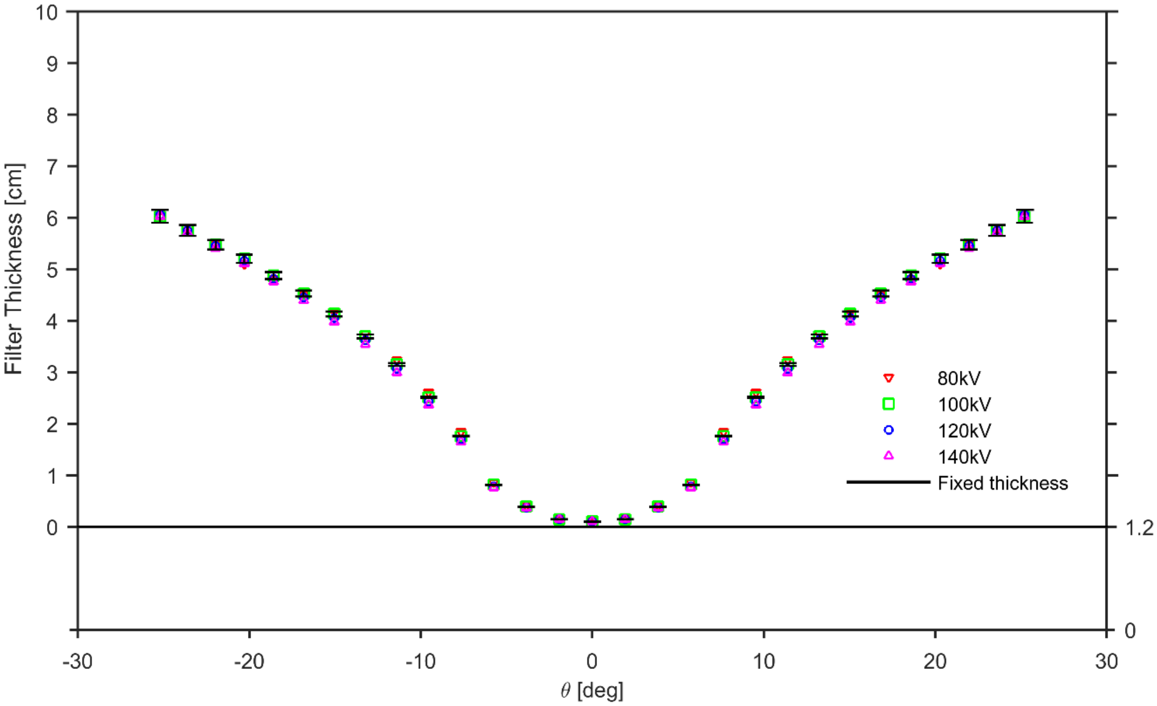

Fig. 9 Calculated BT filter thickness for LFOV at energy levels of 80 kV, 100 kV, 120 kV, and 140 kV. The measured BT filter thickness is shown for aluminum filters (horizontal black line) and Teflon filters (colored lines).

3.5 Monte Carlo simulation

Monte Carlo simulations were executed a total of eight times to simulate static x-ray source. Four simulations were run for energy levels of 80 kV, 100 kV, 120 kV, and 140kV, for both SFOV and LFOV. For each of the conducted simulations, 100 million photon histories were pursued, resulting in coefficients of variance (standard deviation to variance ratio) in the calculated air kerma for each of the ruler holes of less than 0.40 %.

3.5.1 Simulation of the static source geometry for SFOV

Figure 10 shows a normalized attenuation profile of the BT filter obtained from the static x-ray source simulated by MC. This can be directly compared with the BT filter profile measured for a static x-ray source using the CT localizer radiograph for SFOV between the energy levels 80 kV and 140 kV. A strong correlation was observed between the BT profiles of the simulated and the measured air kerma for all measurement points. The RMSE values were 1.64 %, 0.43 %, 0.31 %, and 1.16 % for tube voltages of 80 kV, 100 kV, 120 kV, and 140 kV, respectively.

3.5.2 Simulation of the static source geometry for LFOV

The static x-ray source of the CT localizer radiograph revealed similar agreements for the simulated and measured BT profile results for LFOV, as shown in Fig. 11. The RMSE values were 1.05 %, 1.40 %, 1.80 %, and 2.50 % for tube voltages of 80 kV, 100 kV, 120 kV, and 140 kV, respectively. Significantly, the comparison of the simulated and measured results for both the SFOV and LFOV at all measurement points and tube voltages remained below the 5 % homogeneity threshold of the ionization chamber response.

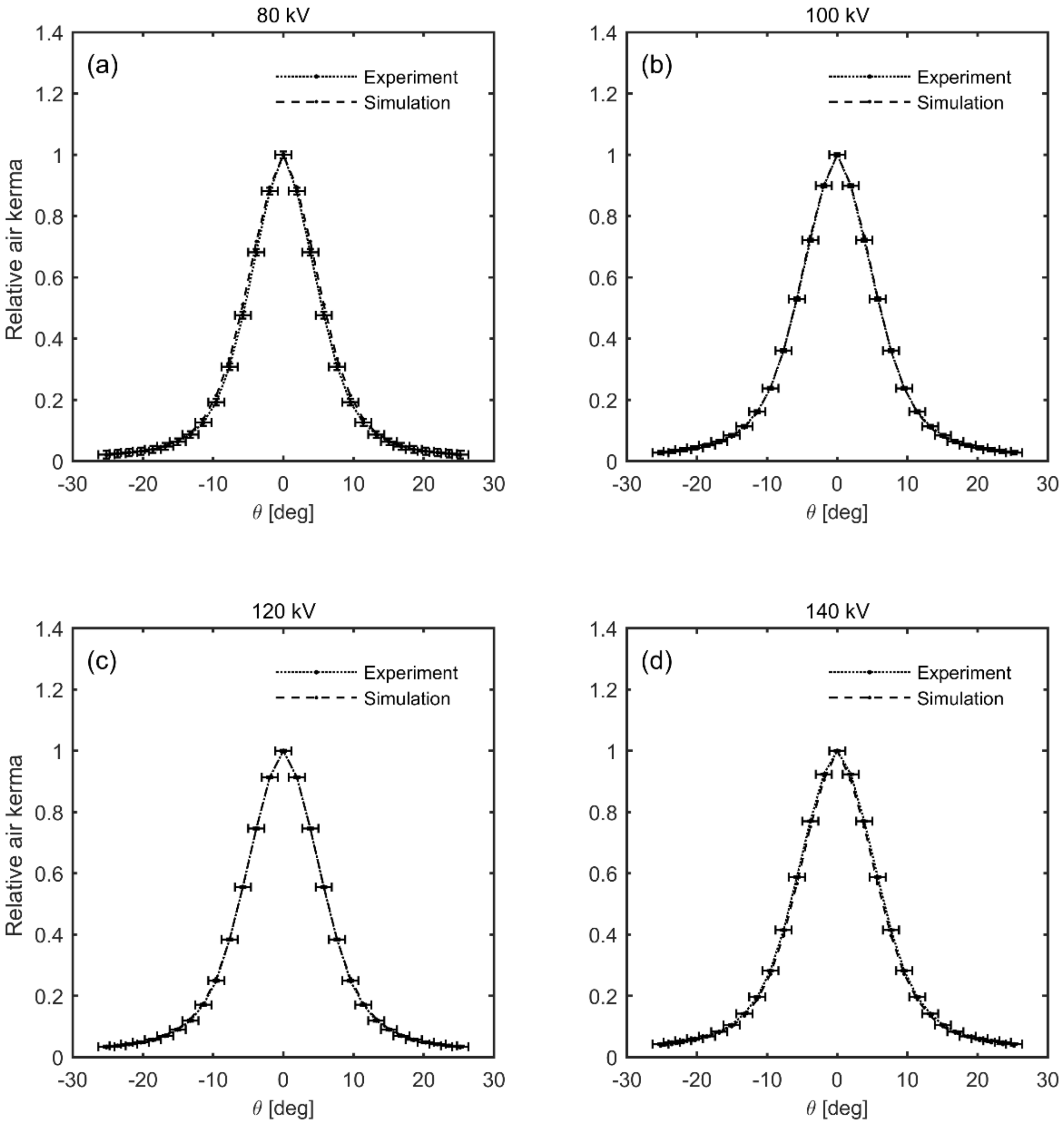

Fig. 10 Comparison of normalized profiles between simulated and measured air kerma of the static x-ray source of the SFOV for (a) 80 kV (b) 100 kV (c) 120 kV (d) 140 kV.

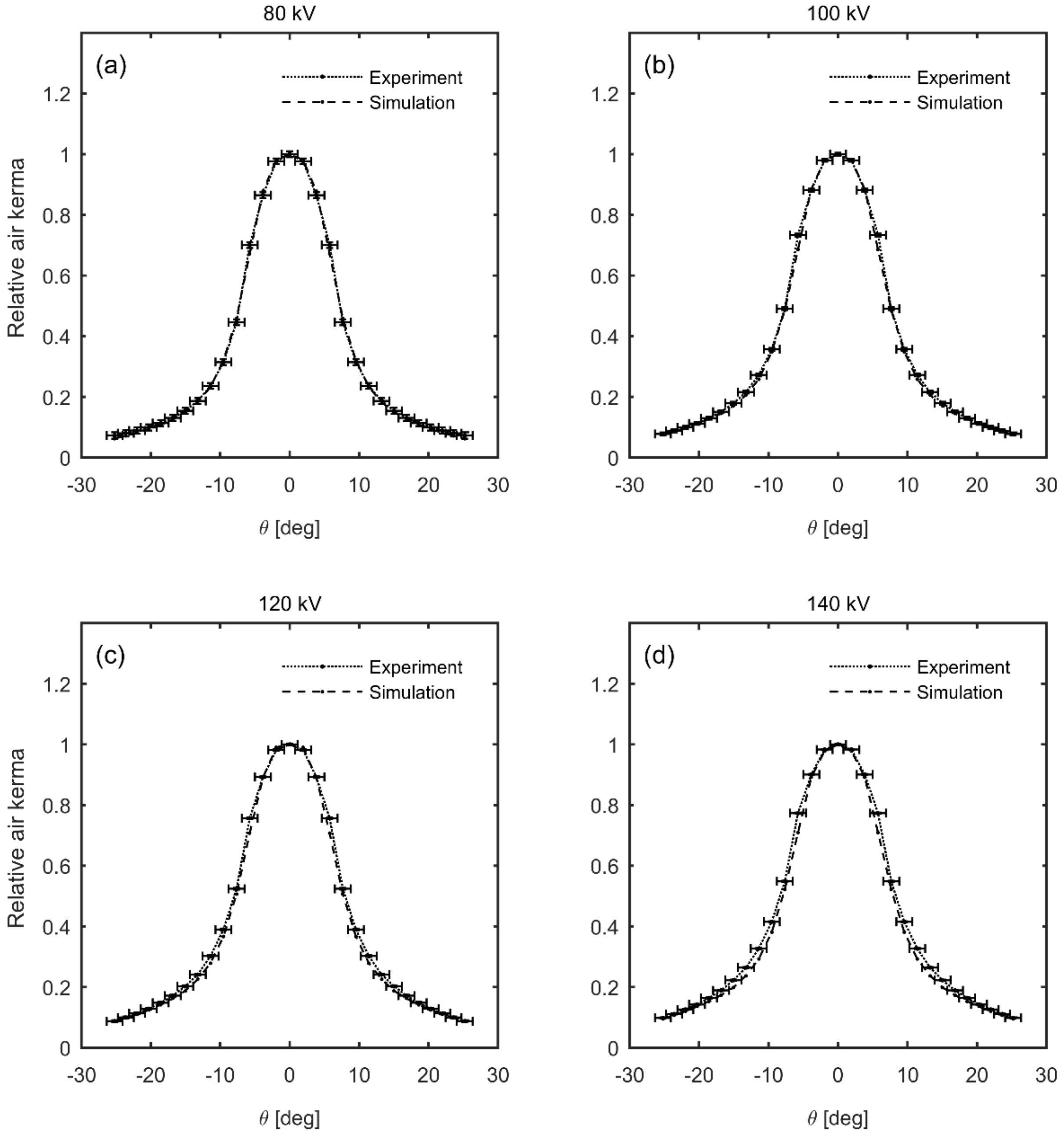

Fig. 11 Comparison of normalized profiles between simulated and measured air kerma of the static x-ray source of the LFOV for (a) 80 kV (b) 100 kV (c) 120 kV (d) 140 kV.

3.5.3 Simulation results for the rotating source geometry for SFOV

The Monte Carlo calculations were carried out for all energy levels and phantoms. Four simulations were run for each computational phantom, each with 100 million photon histories. This resulted in coefficients of variance in the calculated air kerma values for individual holes between 0.40% and 1.0%.

The measurement and simulation data sets were each normalized to the peak value at the top hole. Figures 12 illustrates the relative measured and simulated air kerma of the rotating x-ray source for SFOVs on the standard CTDI body (a, b, c, d), CTDI head (e, f, g, h), and CTDI child (i, j, k, l) phantoms, at tube voltages between 80 kV and 140 kV. The results for the CTDI body phantom revealed a strong correlation between the measured and simulated air kerma for all measurement holes. The maximum deviations were 1.4 %, 4.9 %, 7.2 % and 3.2% for tube voltages of 80 kV, 100 kV, 120 kV, and 140 kV, respectively.

The results for the CTDI head phantom showed similar agreements between the measured and simulated air kerma for all the measurement holes, with maximum deviations of 5.01 %, 1.42 %, 2.85 % and 2.90 % for tube voltages of 80 kV, 100 kV, 120 kV, and 140 kV, respectively.

The results for the CTDI child phantom also showed similar agreements between the simulated and measured air kerma, with maximum deviations of 1.45 %, 3.91 %, 3.15 %, and 3.70 % for tube voltages of 80 kV, 100 kV, 120 kV, and 140 kV, respectively.

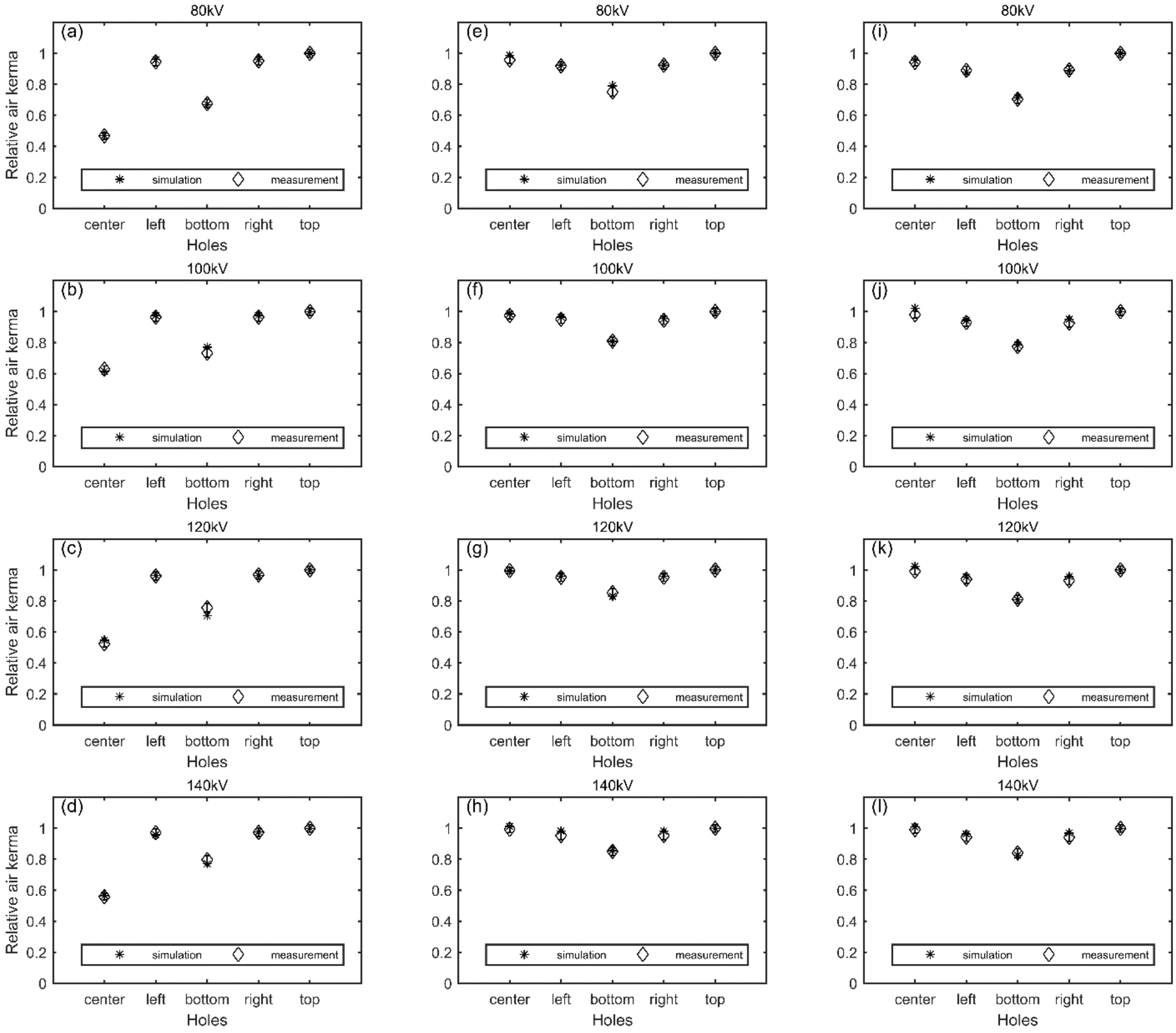

Fig. 12 Comparison of relative measured and simulated air kerma of the CTDI body (a, b, c, d), CTDI head (e, f, g, h), and CTDI child (i, j, k, l) phantoms of the rotating x-ray source for SFOV at tube voltages of 80 kV, 100 kV, 120 kV, and 140 kV.

3.5.4 Simulation results for the rotating source geometry for LFOV

The measurement and simulation data sets were each normalized to the peak value at the top hole. Figure 13 illustrates the relative measured and simulated air kerma of the rotating x-ray source for LFOVs on the standard CTDI body (a, b, c, d), CTDI head (e, f, g, h), and CTDI child (i, j, k, l) phantoms at tube voltages between 80 kV and 140 kV. The measured air kerma of the CTDI body phantom was not significantly different than the simulated air kerma from the MC simulation of the same phantom for all measurement holes. The maximum deviations were 6.01 %, 3.28 %, 2.29 % and 1.7 % for tube voltages of 80 kV, 100 kV, 120 kV, and 140 kV, respectively.

Similar correlations were observed in the results for the CTDI head phantoms for all measurement holes. The maximum deviations were 4.77 %, 2.47 %, 3.36 %, and 3.99 % for tube voltages of 80 kV, 100 kV, 120 kV, and 140 kV, respectively.

The results for the CTDI child phantoms show strong correlations between the measured and simulated air kermas. The maximum deviations were 2.56 %, 5.91 %, 5.74 %, and 6.31 % for tube voltages of 80 kV, 100 kV, 120 kV, and 140 kV, respectively.

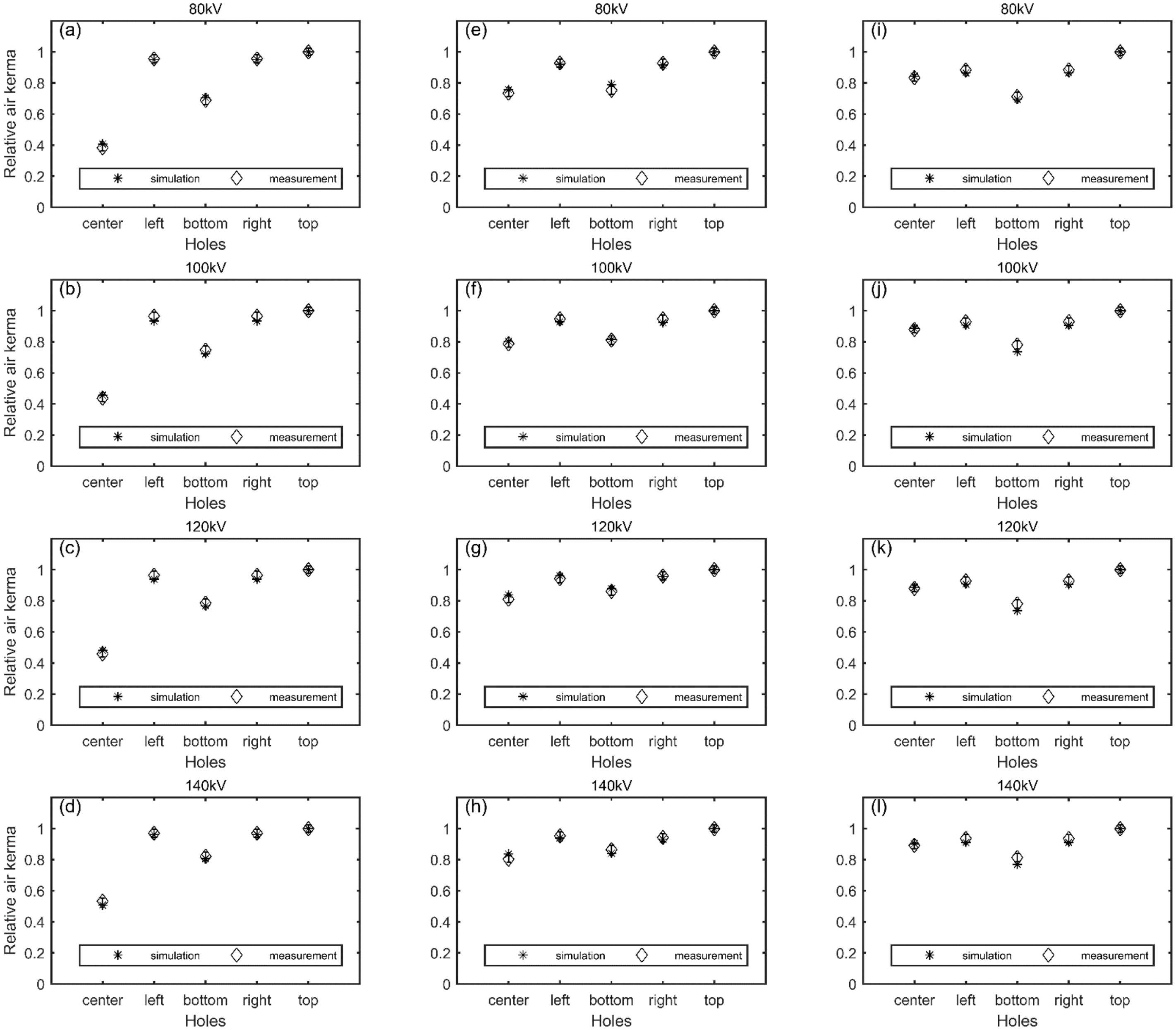

Fig. 13 Comparison of relative measured and simulated air kerma of the CTDI body (a, b, c, d), CTDI head (e, f, g, h), and CTDI child (i, j, k, l) phantoms of the rotating x-ray source for LFOV at tube voltages of 80 kV, 100 kV, 120 kV, and 140 kV.

4 Discussion

The current study attempts to provide an estimation of the BT filter that matches as closely as possible the BT filter utilized by a specific CT scanner. In previous studies, no attempt was made to estimate the thickness of the BT filter using experimental measurements of the CT localizer radiographs of the clinical protocols. The use of a CT localizer radiograph has considerable advantage over the use of the CT scanner in service mode, for which a special personnel agreement is required. In addition to the free accessibility of the static x-ray source, the CT localizer radiograph is a part of the clinical protocol. Hence, it might substantially contribute to the overall radiation dose of full CT scan examinations, particularly in the case of dedicated low-dose scans of young patients, or for screening purposes.[42] This approach could help estimate dose values of the CT localizer radiograph.[43-45]

In this study, the method of integrating the measured attenuation profile of BT filters across the fan angle of the static x-ray source formed the basis of investigating the association between the utilized BT filters in different modes of the scanning process. A strong correlation was observed between the integrated static source of air kerma profiles and the profiles resulting from the measured air kerma of the rotating source of the clinical protocols at a tube voltage of 120 kV.

To test the comprehensiveness of this method, the integrated static x-ray source air kerma profiles based on the physical measurements taken from a particular CT localizer radiograph of the clinical protocol were compared with the air kerma profiles measured from another clinical protocol. This comparison was possible due to the similarity between the FOVs of localizers and clinical protocols. A similar level of agreement was noted between the integrated static x-ray source air kerma profiles based on the CT localizer radiographs of the child neck SFOV and adult abdomen LFOV, as that between the measured air kerma profiles of child abdomen and adult thorax protocols in the case of SFOV and LFOV respectively. These results provide substantial support for the conclusion that the utilized BT filters in the CT localizer radiographs sufficiently represent the thickness and composition of the filters used in clinical protocols. On the other hand, the integration of the static x-ray source method might not result in the same level of consistency as that observed between the integrated and measured profiles in this study if the physical measurements of the static x-ray source made use of the service mode. Additionally, because the service mode is not used in clinical protocols, there is a possibility that the service mode settings are different from the actual settings of the real clinical protocols.

Characterization of the x-ray tube output, as represented by the x-ray spectrum, is essential for an accurate determination of the BT filter thickness at tube voltages of 80, 100, 120 and 140 kV. However, the x-ray spectrum for a given voltage is proprietary, which necessitates an alternative method for estimation. Usually, such methods are based on the principle of HVL measurements, where the HVL is defined as the required thickness of aluminum required to reduce air kerma by one-half. The HVL is energy dependent, and it increases as the x-ray tube potential increases (for example, a tube voltage of 80 KV has a lower HVL than a tube voltage of 140 kV). This results in a more hardened x-ray spectrum for high voltages than for low ones. Therefore, the x-ray spectra generated based on the HVL and used to estimate BT filter thicknesses yield values corresponding to tube voltage. Hence, the resulting attenuation due to BT filter thickness decreases with tube voltage. This could partly explain the discrepancy in the calculated BT filter thickness values for tube voltages of 80 kV, 100 kV, 120 kV, and 140 kV, and the results of MC simulations based on the calculated BT filter thickness in previous studies.[29,31,32]

In this study, the concept of total filtration (TF) was used to estimate the TF thickness at the isocenter independent of tube voltage. The measured TF thickness of the static CT localizer radiograph was 12 mm ± 0.5 mm (Al) for SFOV and LFOV at all tube voltages. These measurements were verified by comparing the measured HVL with the HVL of the x-ray spectra generated by the SpekCalc program. The TF thicknesses measured by the Nomex multimeter device were found to be in good agreement with the resulting TF thicknesses generated by the SpekCalc program that resulted from the measured HVL values at each energy level of 80 kV - 140 kV for SFOV and LFOV. For SFOV the maximum percentage difference was 2.53 % at 80 kV and the minimum percentage difference was 0.42 % at both 120 kV and 140 kV. For LFOV the maximum percentage difference was 1.68 % at 80 kV, and 0.42 % at both 100kV and 120kV. A similar result was found in an earlier study where researchers observed a total beam filtration of up to 12mm for A1 equivalent filtration in the CT scanners.[46] The x-ray spectra generated using the TF thickness were used to calculate the BT filter thickness for each tube voltage. This could explain why the calculated BT filter thickness was the same for all energy levels. This consistency, in turn, provides support for the hypothesis that BT filter thickness is dependent on energy level and, more specifically, the FOV. The slight deviation observed in the calculated BT filter thickness could be the result of measurement error of the localizer radiographs, along with the 10 % uncertainty stemming from the algorithm utilized in calculating the BT filter thickness.

The accuracy of the x-ray spectrum and the estimated BT filter thickness of the x-ray tube are essential to effectively compare the calculated air kerma from the MC simulation with the measured air kerma from the experiments. In addition, a substantial geometrical correlation is also required between the dosimetry phantoms and the computational model. In the current study, the simulated air kerma and the measured air kerma of the static x-ray source showed strong agreement at each tube voltage. The RMSE values across all the measurement angles for both SFOV and LFOV fall within the functionality of the ionization chamber with a 5 % uncertainty for all tube voltages between 80 kV and 140 kV. This indicates that the calculated BT filter thicknesses correspond to those of the given CT scanner. Moreover, the x-ray spectrum SpekCalc software, which is based on the measured TF at the isocenter, gives a good approximation of the x-ray tube's output.

The calculated BT filter thickness of the rotating x-ray source showed significant agreement with both the simulated and measured SFOVs across all measurement holes. The maximum deviation of 7.2 % was observed at 120 kV for the CTDI body phantom. A similar correspondence was found between the simulated and measured air kerma for LFOV. Here, the maximum deviations observed across all measurement holes of the CTDI body phantom were less than 6.01 % at 80 kV and less than 5.91 % at 140 kV for the CTDI child phantom. This level of uncertainty could be attributed to measurement error, or error due to external factors such as variations in temperature, pressure, and x-ray source output. An additional reason for the deviation between the simulated and measured air kerma could be the combined effects of using a geometry voxel representation-based MC, and the MC source code.

5 Conclusion

The integration method described in this study successfully resulted in an accurate estimation of the BT profile for the rotating x-ray source based on the measured BT profile of the static x-ray source. This suggests that the integration method can result in a very strong correlation between the integrated and measured profiles. This indicates the possibility of deducing the BT filter thickness of the clinical protocol based on the physical measurements of the CT localizer radiograph alone. The physical measurements, along with the calculations, were adequate to estimate an accurate BT filter thickness for each energy spectrum that was attenuated by the TF thickness. The strong correlation between the simulated and actual physical measurements of air kerma for both the static and rotating x-ray sources supports this conclusion. These results will help to more accurately estimate the dose delivered to specific organs of the body, and thereby contribute to cancer risk management in diagnostic radiology.

Disclosures

No conflicts of interest

Acknowledgments

The authors gratefully acknowledge a grant by “Deutscher Akademischer Austauschdienst” (DAAD, German Academic Exchange Service, Germany, grant program number: 57048249.

References

1. C. H. McCollough, G. H. Chen, W. Kalender, S. Leng, E. Samei, K. Taguchi, G. Wang, L. Yu, and R. I. Pettigrew, “Achieving routine submil-lisievert CT scanning: Report from the summit on management of radiation dose in CT,” *Radiology*. **264**(2), 567–580 (2012).
2. D. J. Brenner and E. J. Hall, “Computed tomography–An increasing source of radiation exposure,” *N. Engl. J. Med*. **357**(22), 2277–2284 (2007).
3. F. A. Mettler, Jr., M. Bhargavan, K. Faulkner, D. B. Gilley, J. E. Gray, G. S. Ibbott, J. A. Lipoti, M. Mahesh, J. L. McCrohan, M. G. Stabin, B. R. Thomadsen, and T. T. Yoshizumi, “Radiologic and nuclear medicine studies in the United States and worldwide: Frequency, radiation dose, and comparison with other radiation sources–1950–2007,” *Radiology*. **253**(2), 520–531 (2009).
4. NCRP report no. 160, Ionizing radiation exposure of the population of the United States (National Council on Radiation Protection and Measurements, Bethesda, MD, 2009).
5. BEIR VII report, Health Risks from Exposure to Low Levels of Ionizing Radiation. BEIR VII Phase 2 (National Academies Press, Washington, DC, 2006).
6. Parisa Akhlaghi, Elie Hoseinian-Azghadi, Hashem Miri-Hakimabad, and Laleh Rafat- Motavalli, “A Monte Carlo study on quantifying the amount of dose reduction by shielding the superficial organs of an Iranian 11-year-old boy,” *J Med Phys*. **41**(4), 246–253 (2016).
7. Jarry G, DeMarco JJ, Beifuss U, Cagnon CH, McNitt-Gray MF.,“ A Monte Carlo-based method to estimate radiation dose from spiral CT: from phantom testing to patient-specific models,” *Phys Med Biol*. **48**(16), 2645-63 (2003).
8. Salvadó M, López M, Morant JJ, Calzado A., “ Monte Carlo calculation of radiation dose in CT examinations using phantom and patient tomographic models,” *Radiat Prot Dosimetry*. **114**(1-3), 364-8 (2005).

9. DeMarco JJ, Cagnon CH, Cody DD, Stevens DM, McCollough CH, O'Daniel J, McNitt-Gray MF. , “A Monte Carlo based method to estimate radiation dose from multidetector CT (MDCT): cylindrical and anthropomorphic phantoms,” *Phys Med Biol*. **50**(17): 3989-4004 (2005).

10. Caon M., “ The reduction in Monte Carlo calculated organ doses from CT with tube current modulation using WILLIAM, a voxel model of seven year-old anatomy,” *Australas Phys Eng Sci Med*. **37**(4):743-52 (2014).

11. AJ Einstein et al., “Radiation dose and cancer risk estimates in 16-slice computed tomography coronary angiography,” *J Nucl Cardiol*. **15**(2), 232–240 (2008).

12. A. C. Turner et al., “The feasibility of a scanner-independent technique to estimate organ dose from MDCT scans: Using CTDIvol to account for differences between scanners,” *Med Phys*. **37**(4), 1816–1825 (2010).

13. Li X, Samei E, Segars WP, Sturgeon GM, Colsher JG, Frush DP., “ Patient-specific radiation dose and cancer risk for pediatric chest CT,” *Radiology*. **259**(3),862-74 (2011).

14. Li X, Samei E, Segars WP, Sturgeon GM, Colsher JG, Toncheva G, Yoshizumi TT, Frush DP., “ Patient-specific radiation dose and cancer risk estimation in CT: part II. Application to patients,” *Med Phys*. **38**(1),408-19 (2011).

15. Oono T, Araki F, Tsuduki S, Kawasaki K., “ Monte Carlo calculation of patient organ doses from computed tomography,” *Radiol Phys Technol*. **7**(1),176-82 (2014).

16. H. Zaidi and M. R. Ay, “Current status and new horizons in Monte Carlo simulation of x-ray CT scanners,” *Med. Biol. Eng. Comput*, **45**(9), 809–817(2007).

17. M. R. Ay and H. Zaidi., "Development and validation of MCNP4C-based Monte Carlo simulator for fan- and cone-beam x-ray CT," *Phys. Med.Biol.* **50**(20), 4863–4885 (2005).

18. D M Tucker, G T Barnes, and D P Chakraborty., "Semiempirical model for generating tungsten target x-ray spectra," *Medical Physics*, **18** (2), 211–218 (1991).

19. A. C. Turner et al., “A method to generate equivalent energy spectra and filtration models based on measurement for multidetector CT Monte Carlo dosimetry simulations,” *Med. Phys.* **36**(6), 2154 (2009).

20. J. M. Boone., “Method for evaluating bow tie filter angle-dependent attenuation in CT: Theory and simulation results,” *Med. Phys.* **37**(1), 40–48 (2010).

21. SE McKenney et al., “Experimental validation of a method characterizing bow tie filters in CT scanners using a real-time dose probe,” *Med. Phys.* **38** (3), 1406 (2011).

22. BR Whiting et al., “Measurement of bow tie profiles in CT scanners using a real-time dosimeter,” *Med. Phys.* **41**(10), 101915 (2014).

23. M Randazzo, M Tambasco. , “A rapid noninvasive characterization of CT x-ray sources,” *Med Phys.* **42**(7), 3960–3968 (2015).

24. Y. Poirier, A. Kouznetsov, B. Koger, and M. Tambasco, “Experimental validation of a kilovoltage x-ray source model for computing imaging dose,” *Med. Phys.* **41**(4), 041915 (2014).

25. Lin Y, Ramirez-Giraldo JC Gauthier DJ, Stierstorfer K, Samei E., “An angle-dependent estimation of CT x-ray spectrum from rotational transmission measurements,” *Med. Phys.* **41**(6), 062104, (2014).

26. Kai Yang, Xinhua Li, X. George Xu, Bob Liu, “Direct and fast measurement of CT beam filter profiles with simultaneous geometrical calibration,” Med. Phys. **44**(1), 57-70, (2017).

27. M Randazzo, M Tambasco. , “A rapid noninvasive characterization of CT x-ray sources,” *Med Phys.* **42**(7), 3960–3968 (2015).

28. K. McMillan, M. McNitt-Gray, and D. Ruan, “Development and validation of a measurement-based source model for kilovoltage cone-beam CT Monte Carlo dosimetry simulations,” *Med. Phys.* **40**(11), 111907 (2013).

29. B Alikhani, L Büermann., “Non-invasive experimental determination of a CT source model,” *Phys Med.* **32**(1), 59-66 (2016).

30. Sommerville M, Poirier Y, Tambasco M1., “A measurement-based X-ray source model characterization for CT dosimetry computations,” *J Appl Clin Med Phys*. **16**(6):386-400 (2015).

31. X Lopez-Rendon et al., “Implementing the complete beam hardening effect of the bowtie filter versus scaling beam intensities: effects on dosimetric applications in computed tomography,” *J Med Imaging (Bellingham)*. **1**(3), 0091-3286 (2014).

32. X Li et al., “A new technique to characterize CT scanner bow-tie filter attenuation and applications in human cadaver dosimetry simulations,” *Med Phys.* **42** (11). 6274-6282 (2015).

33. Center for Evidence_Based Purchasing CEP, “Comparative specifications 32 to 40 slice CT scanners,” Report No. CEP08026 (NHSPASA, London, UK, 2009).

34. PTW Freiburg GmbH, " CT Chambers Type 30009," PTW, 22 February 2017. [http://www.ptw.de/fileadmin/data/download/catalogviewer/DETECTORS_Cat_en_16522900_10/blaetterkatalog/index.html?startpage=38#page_38].

35. IEC 61674: International Electrotechnical Commission. Medical electrical equipment-Dosemeters with ionization chambers and/or semiconductor detectors as used in X-ray diagnostic imaging.

36. PTW Freiburg GmbH, " NOMEX PTB Type Approved," PTW, 14 February 2012. [http://www.ptw.de/1861.html?&no_cache=1&tx_ttnews%5Btt_news%5D=132].

37. PTW Freiburg GmbH, " True Precision. PTW. NOMEX® Multimeter," PTW, 03 February 2017. [http://www.ptw.de/2361.html?&cId=7082%22%27%60—].

38. PTW Freiburg GmbH," NOMEX Multimeter," PTW, 03 February 2017. [http://www.ptw.de/2362.html?&cId=7082%22%27%60--].

39. G. Poludniowski et al., “SpekCalc: A program to calculate photon spectra from tungsten anode x-ray tubes,” *Phys. Med. Biol.* **54**(19), N433–N438 (2009).

40. R Schmidt,J Wulff,K Zink.,“ GMctdospp: Description and validation of a CT dose calculation system,” *Med. Phys.* **42** (7). 4260-4270 (2015).

41. I. Kawrakow, E. Mainegra-Hing, D. W. O. Rogers, F. Tessier, and B. R. B. Walters, “The EGSnrc code system: Monte Carlo simulation of electron and photon transport,” NRC Report No. PIRS-701 (National Research Council of Canada, Ottawa, 2013).

42. B Schmidt, N Saltybaeva, D Kolditz, WA Kalender., “Assessment of patient dose from CT localizer radiographs,” *Med Phys.* **40**(8), 084301 (2013).

43. D. R. Coles et al., “Comparison of radiation doses from multislice computed tomography coronary angiography and conventional diagnostic angiography,” *J. Am. Coll. Cardiol.* **47** (9), 1840–1845 (2006).

44. J. C. O'Daniel, D. M. Stevens, and D. D. Cody, "Reducing radiation exposure from survey CT scans," *AJR, Am. J. Roentgenol.* **185** (2), 509–515 (2005).

45. K. Perisinakis, J. Damilakis, A. Voloudaki, A. Papadakis, and N. Gourt-soyiannis, "Patient dose reduction in CT examinations by optimizing scanogram acquisition," *Radiat. Prot. Dosim.* **93** (2), 173–178 (2001).

46. Nagel HD. *CT parameters that influence the radiation dose: radiation dose from adults and pediatric multidetector computed tomography*. Berlin, Germany: Springer-Verlag, pp 51–79 (2007).

First Author is currently a PhD student at the Otto von Guericke Universität Magdeburg, Germany. He received his BSc degree in radiation science from the University of Science and Technology in Jordan, and his master degree in medical science from Örebro University, Sweden in 2008, 2013, respectively. His PhD subject focuses on the dosimetry calculation of organ dose in computed tomography.

Biographies and photographs for the other authors are not available.

<u>Caption List</u>

Fig. 1 The Nomex multimeter active area in the measurement of the total filtration for CT scan.

Fig. 2 Schematic view of BT profile measurements across the fan angle of the static x-ray source.

Fig. 3 Experimental set up of HVL measurements.

Fig. 4 Experimental scheme of BT profile measurements of attenuation of the rotating x-ray source of the clinical protocols.

Fig. 5 Schematic view of the geometrical relationship between a static x-ray source and the integrated static x-ray source resulting from the integration method.

Fig. 6 Comparison of normalized profiles of BT filter from the integrated air kerma and the measured air kerma for the SFOV at 120 kV. (a) Static source integrated and child neck protocol. (b) Static source integrated and child abdomen protocol.

Fig. 7 Comparison of normalized profiles of BT filter from the integrated air kerma and the measured air kerma for the LFOV at 120 kV. (a) Static source integrated and adult thorax protocol. (b) Static source integrated and adult abdomen protocol.

Table 1. Measured TF thickness in mm Al from the Nomex multimeter device and the resulting TF thickness in mm Al from the SpekCalc program, resulting from matching the measured HVL in mm Al for all tube voltages ranging from 80 kV to 140 kV for SFOV.

Table 2. Measured TF thickness in mm Al from the Nomex multimeter device and the resulting TF thickness in mm Al from the SpekCalc program, resulting from matching the measured HVL in mm Al for all tube voltages ranging from 80 kV to 140 kV for LFOV.

Fig. 8 Calculated BT filter thickness for SFOV at energy levels of 80 kV, 100 kV, 120 kV, and 140 kV. The measured BT filter thickness is shown for aluminum filters (horizontal black line) and Teflon filters (colored lines).

Fig. 9 Calculated BT filter thickness for LFOV at energy levels of 80 kV, 100 kV, 120 kV, and 140 kV. The measured BT filter thickness is shown for aluminum filters (horizontal black line) and Teflon filters (colored lines).

Fig. 10 Comparison of normalized profiles between simulated and measured air kerma of the static x-ray source of the SFOV for (a) 80 kV (b) 100 kV (c) 120 kV (d) 140 kV.

Fig. 11 Comparison of normalized profiles between simulated and measured air kerma of the static x-ray source of the LFOV for (a) 80 kV (b) 100 kV (c) 120 kV (d) 140 kV.

Fig. 12 Comparison of relative measured and simulated air kerma of the CTDI body (a, b, c, d), CTDI head (e, f, g, h), and CTDI child (i, j, k, l) phantoms of the rotating x-ray source for SFOV at tube voltages of 80 kV, 100 kV, 120 kV, and 140 kV.

Fig. 13 Comparison of relative measured and simulated air kerma of the CTDI body (a, b, c, d), CTDI head (e, f, g, h), and CTDI child (i, j, k, l) phantoms of the rotating x-ray source for LFOV at tube voltages of 80 kV, 100 kV, 120 kV, and 140 kV.

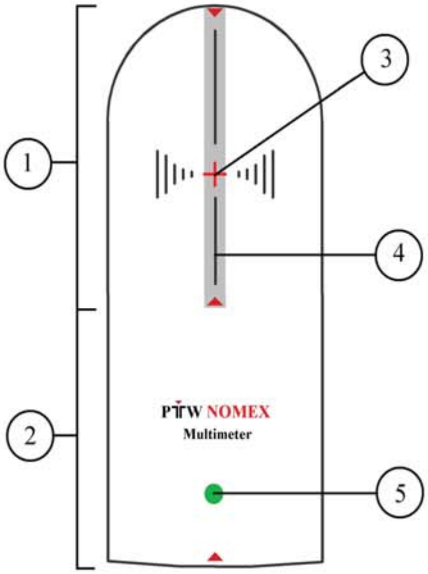
1
2
3
4
5
PTW NOMEX
Multimeter

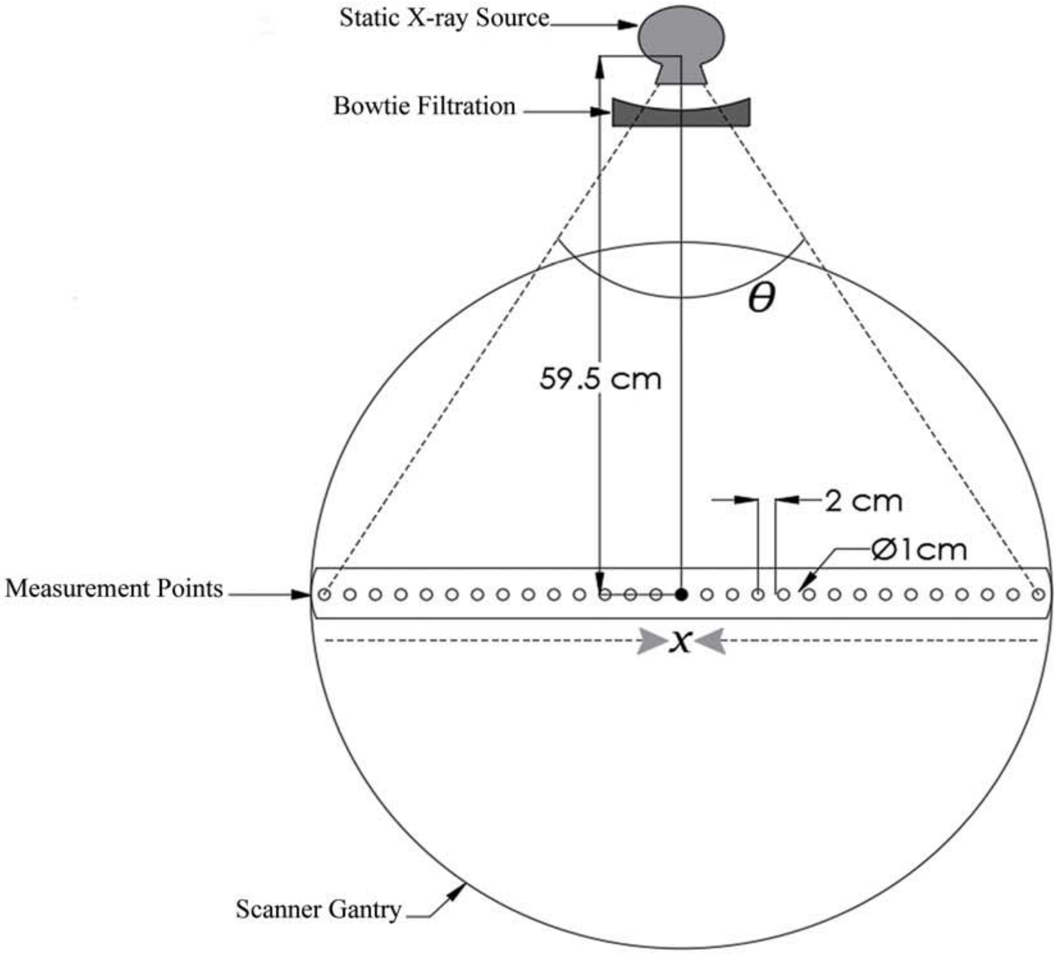
Static X-ray Source
Bowtie Filtration
θ
59.5 cm
2 cm
Ø1cm
Measurement Points
x
Scanner Gantry

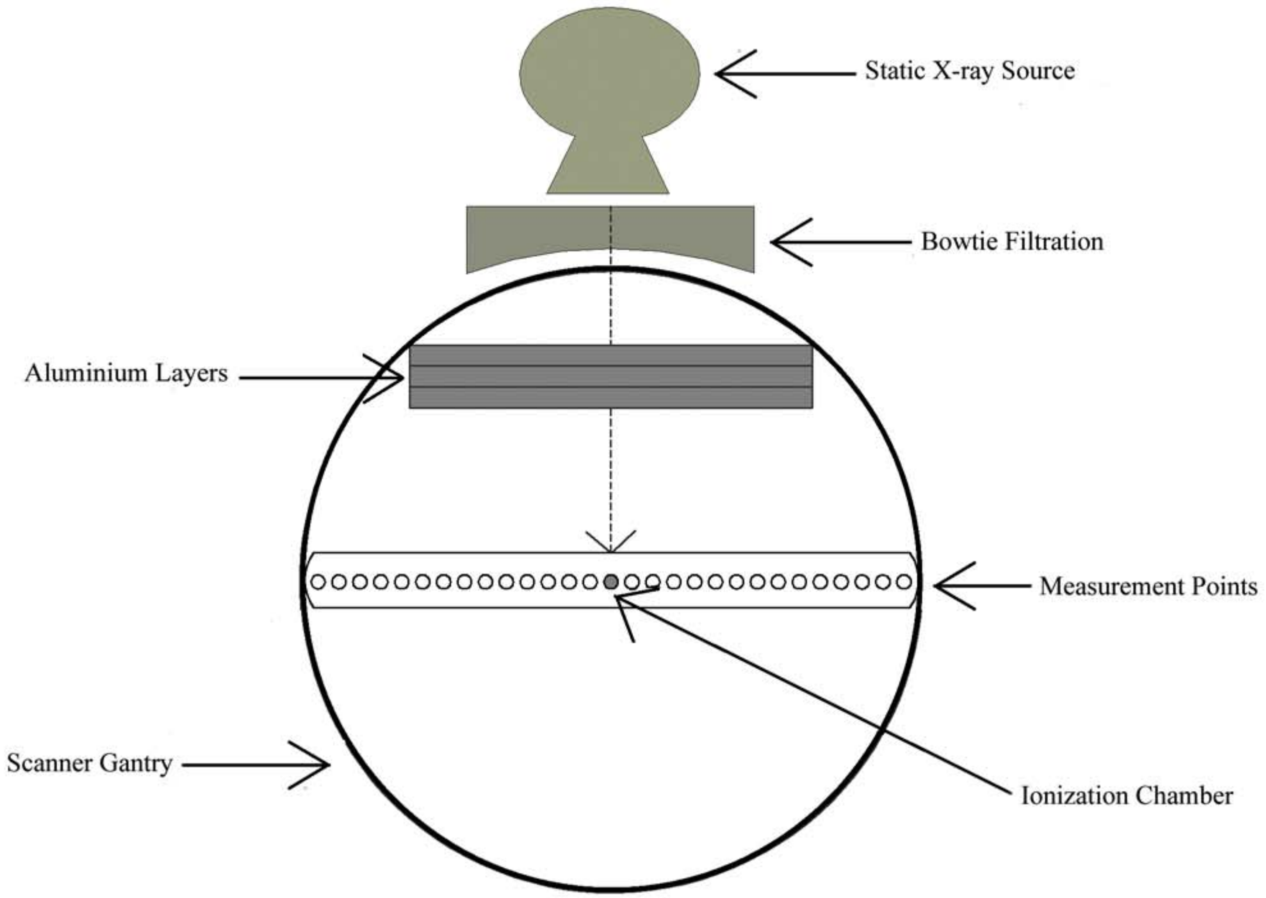
Static X-ray Source
Bowtie Filtration
Aluminium Layers
Measurement Points
Scanner Gantry
Ionization Chamber

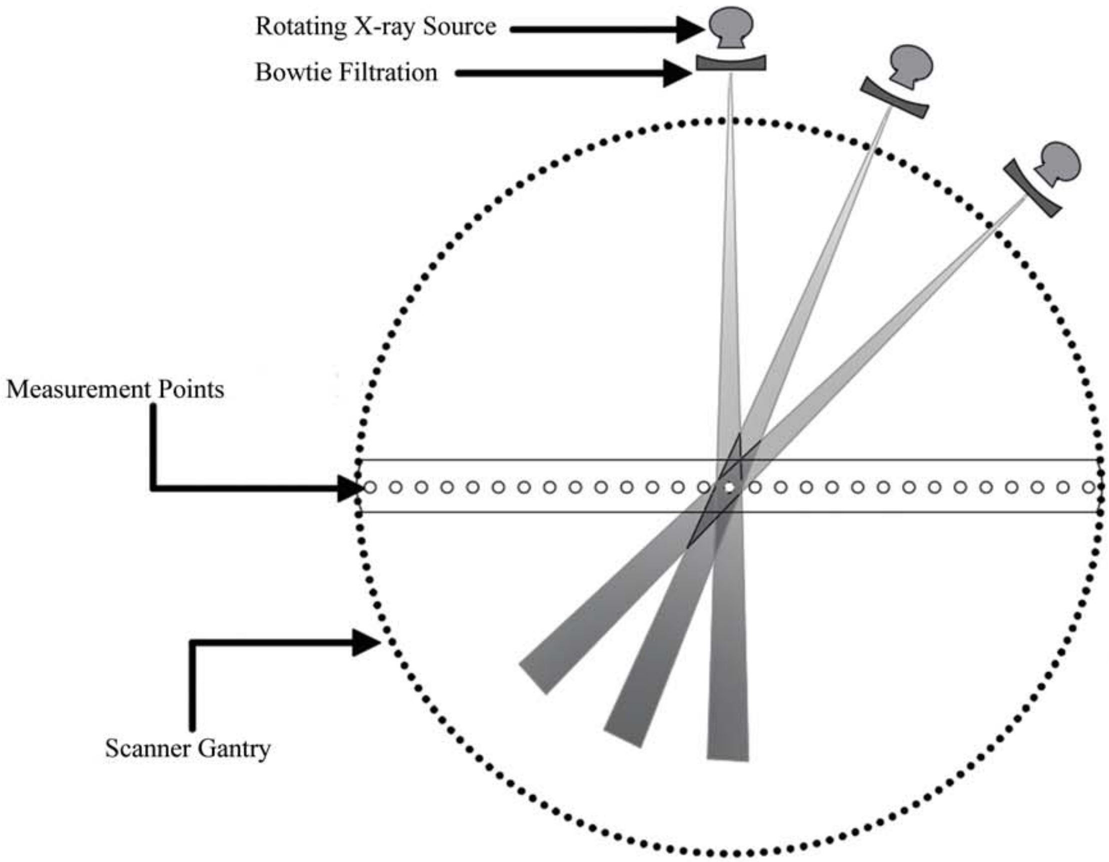
Rotating X-ray Source
Bowtie Filtration
Measurement Points
Scanner Gantry

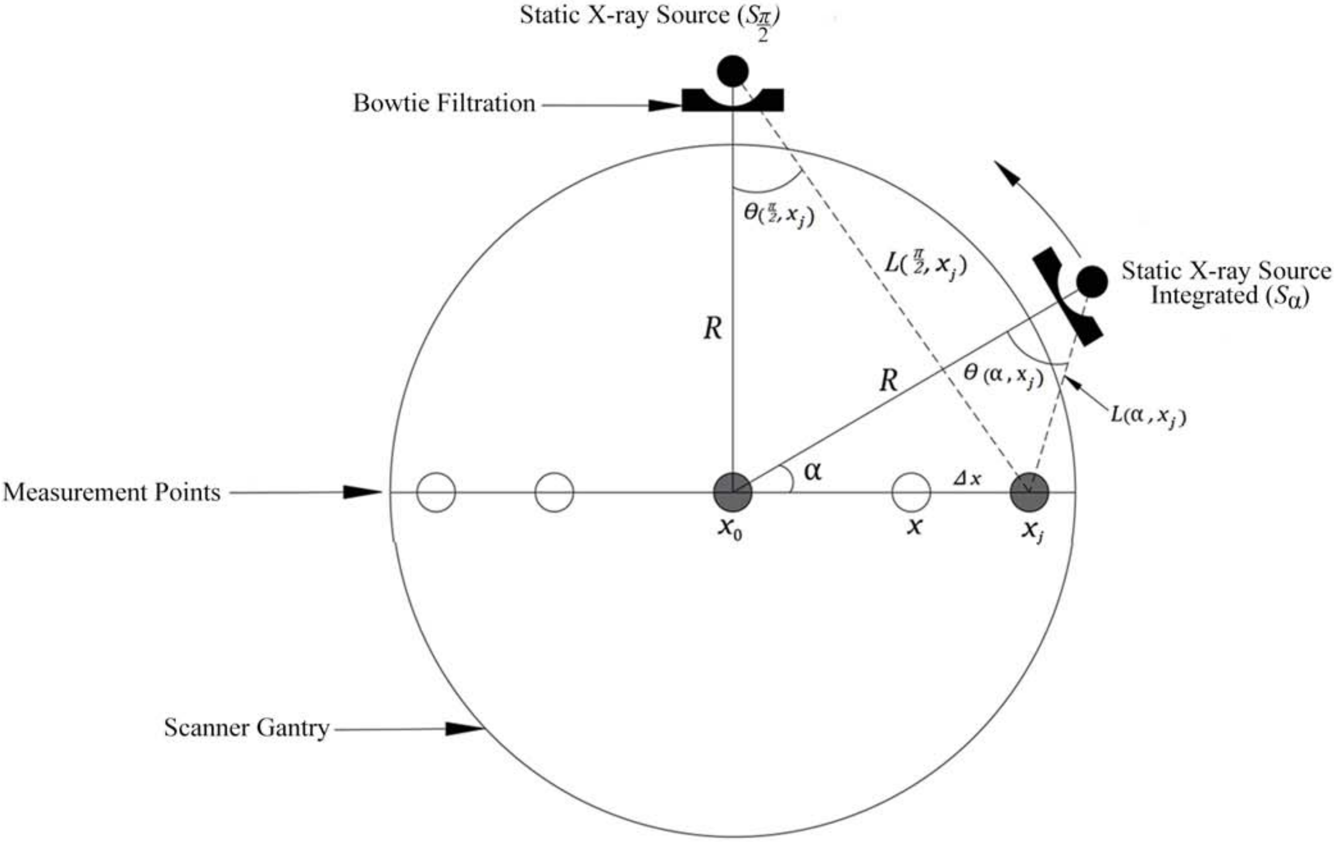

Static X-ray Source ($S_{\frac{\pi}{2}}$)
Bowtie Filtration
$\theta(\frac{\pi}{2}, x_j)$
$L(\frac{\pi}{2}, x_j)$
Static X-ray Source
Integrated (S_α)
R
R
$\theta(\alpha, x_j)$
$L(\alpha, x_j)$
Measurement Points
α
Δx
x_0
x
x_j
Scanner Gantry

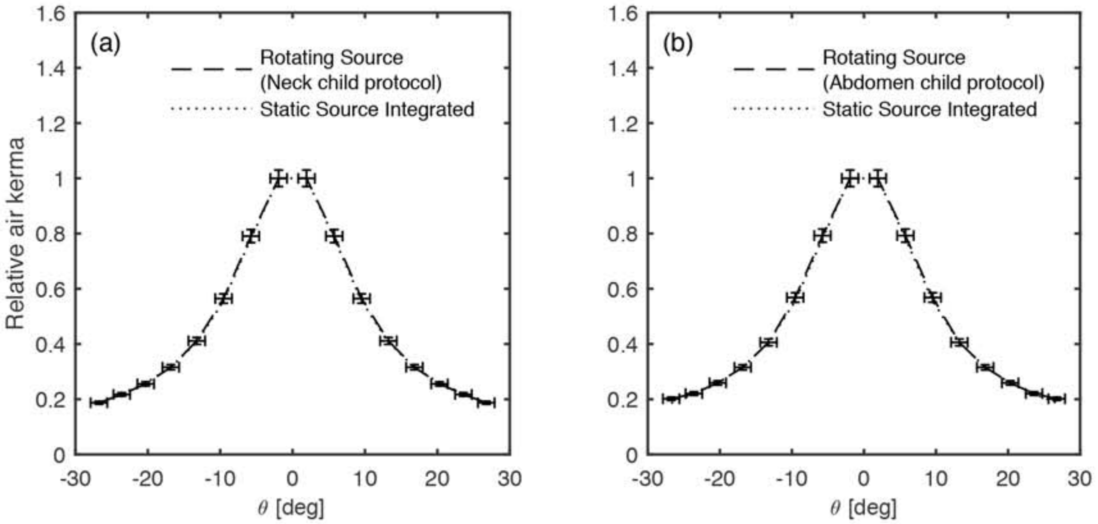
(a)
Rotating Source
(Neck child protocol)
Static Source Integrated
Relative air kerma
0
0.2
0.4
0.6
0.8
1
1.2
1.4
1.6
-30
-20
-10
0
10
20
30
θ [deg]
(b)
Rotating Source
(Abdomen child protocol)
Static Source Integrated
0
0.2
0.4
0.6
0.8
1
1.2
1.4
1.6
-30
-20
-10
0
10
20
30
θ [deg]

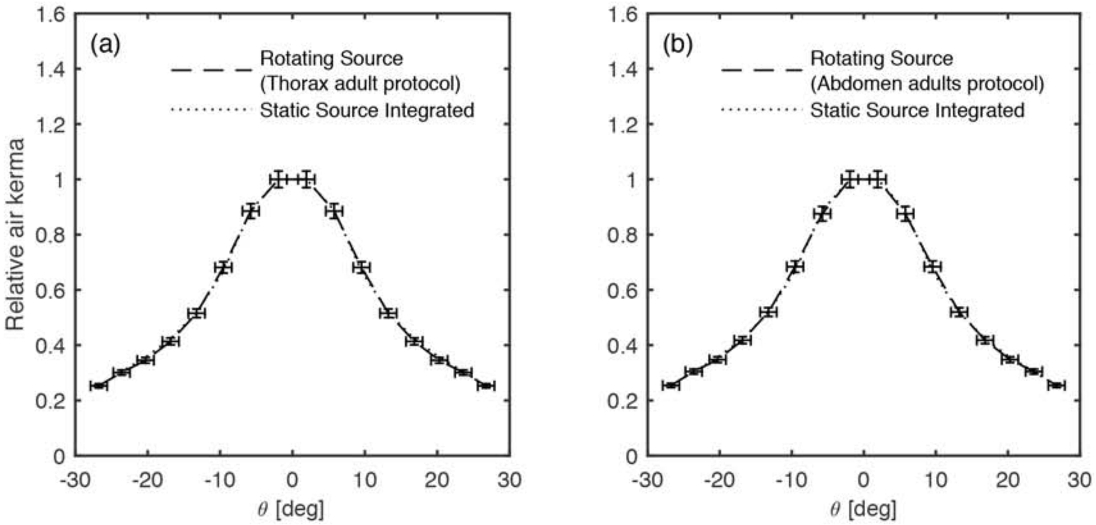
(a)
Rotating Source
(Thorax adult protocol)
Static Source Integrated
Relative air kerma
1.6
1.4
1.2
1
0.8
0.6
0.4
0.2
0
-30
-20
-10
0
10
20
30
θ [deg]
(b)
Rotating Source
(Abdomen adults protocol)
Static Source Integrated
1.6
1.4
1.2
1
0.8
0.6
0.4
0.2
0
-30
-20
-10
0
10
20
30
θ [deg]

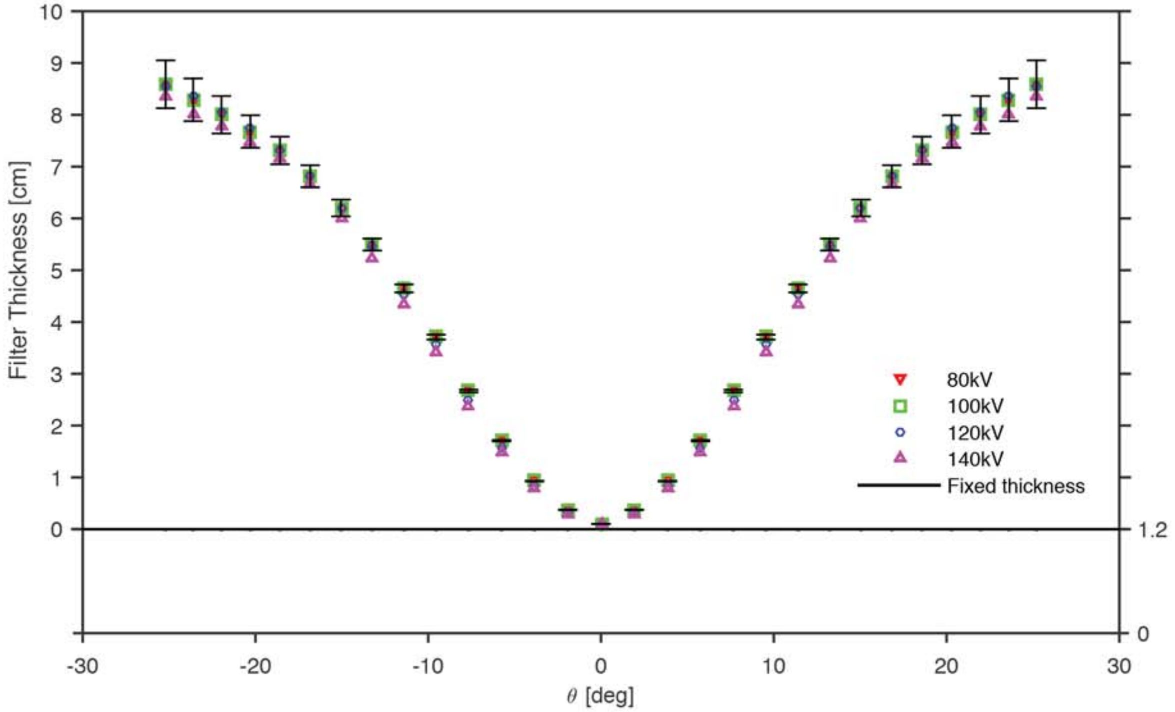
Filter Thickness [cm]
10
9
8
7
6
5
4
3
2
1
0
1.2
0
-30
-20
-10
0
10
20
30
θ [deg]
80kV
100kV
120kV
140kV
Fixed thickness

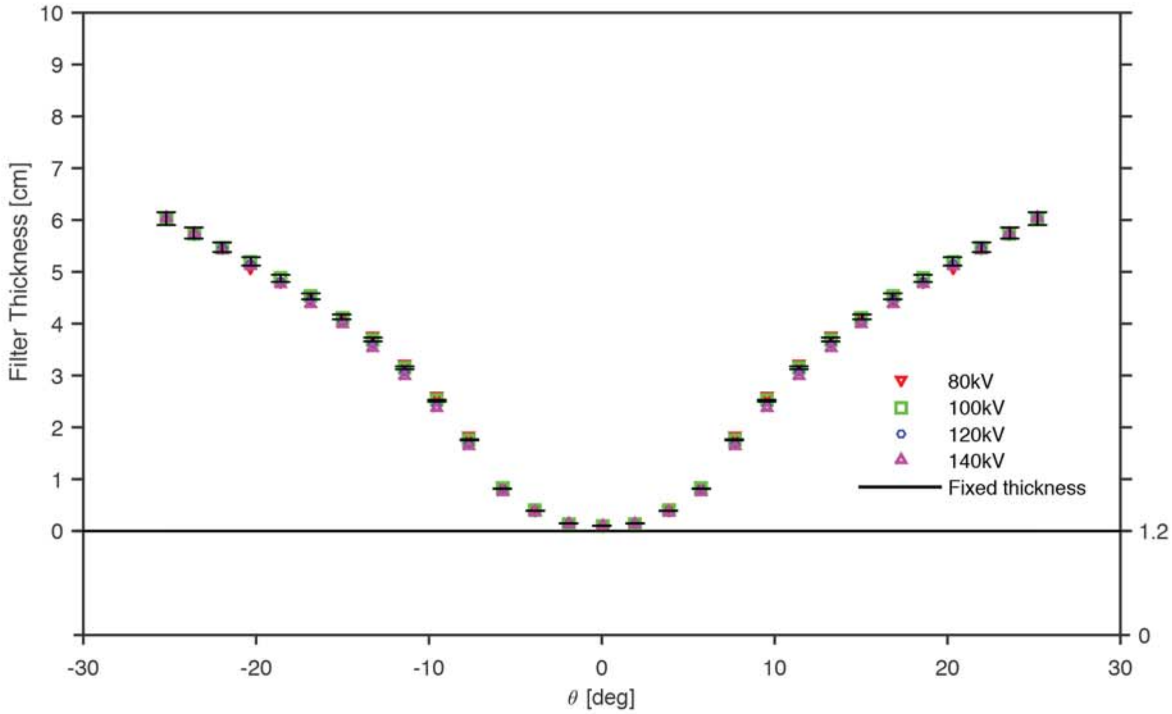
Filter Thickness [cm]
10
9
8
7
6
5
4
3
2
1
0
1.2
0
-30
-20
-10
0
10
20
30
θ [deg]
80kV
100kV
120kV
140kV
Fixed thickness

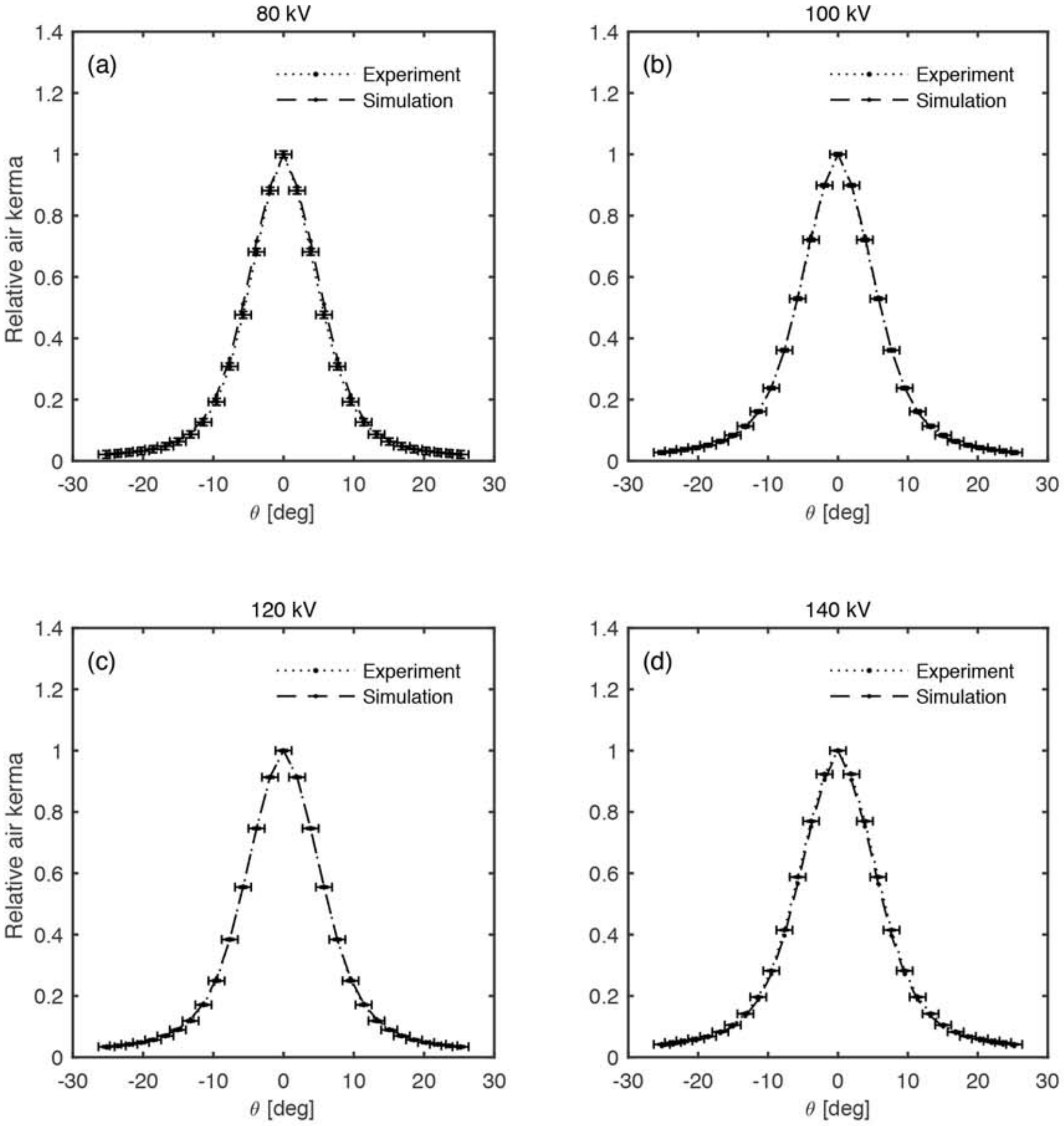

80 kV
100 kV
120 kV
140 kV
(a)
(b)
(c)
(d)
Experiment
Simulation
Relative air kerma
θ [deg]
0
0.2
0.4
0.6
0.8
1
1.2
1.4
-30
-20
-10
0
10
20
30

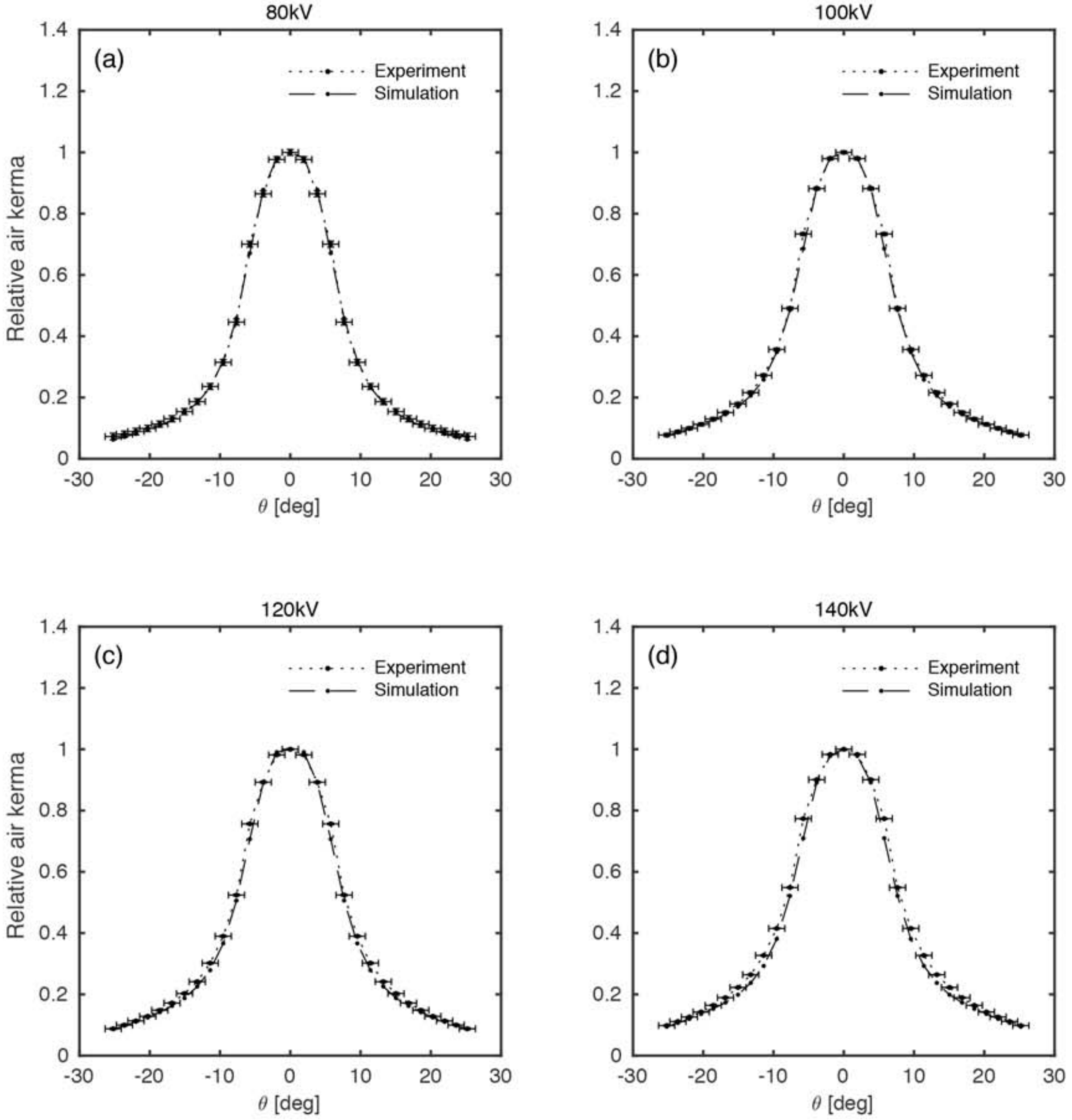
80kV
(a)
100kV
(b)
120kV
(c)
140kV
(d)
Experiment
Simulation
Relative air kerma
θ [deg]
0
0.2
0.4
0.6
0.8
1
1.2
1.4
-30
-20
-10
0
10
20
30

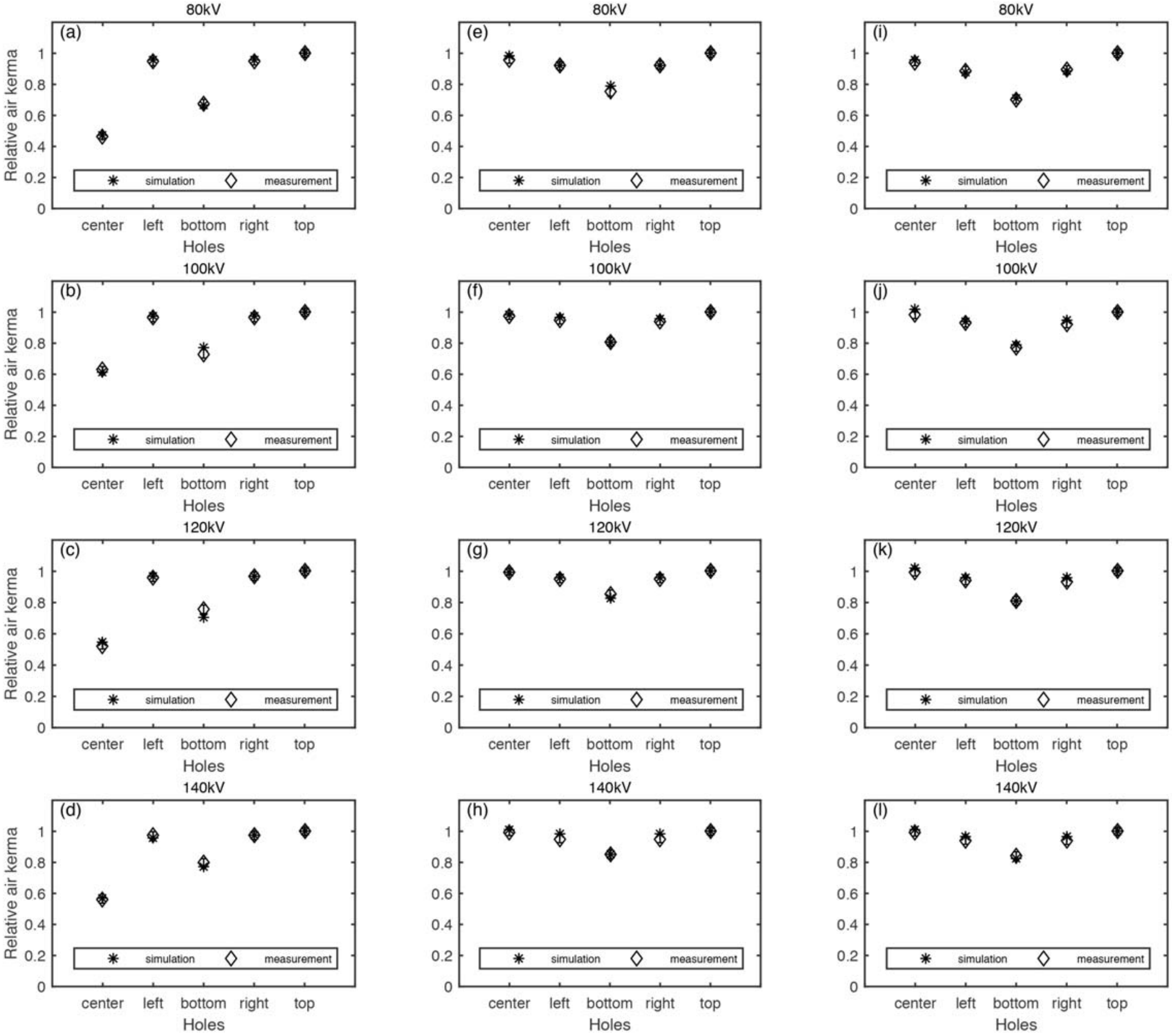
80kV
(a)
(e)
(i)
100kV
(b)
(f)
(j)
120kV
(c)
(g)
(k)
140kV
(d)
(h)
(l)
Relative air kerma
0
0.2
0.4
0.6
0.8
1
simulation
measurement
center
left
bottom
right
top
Holes

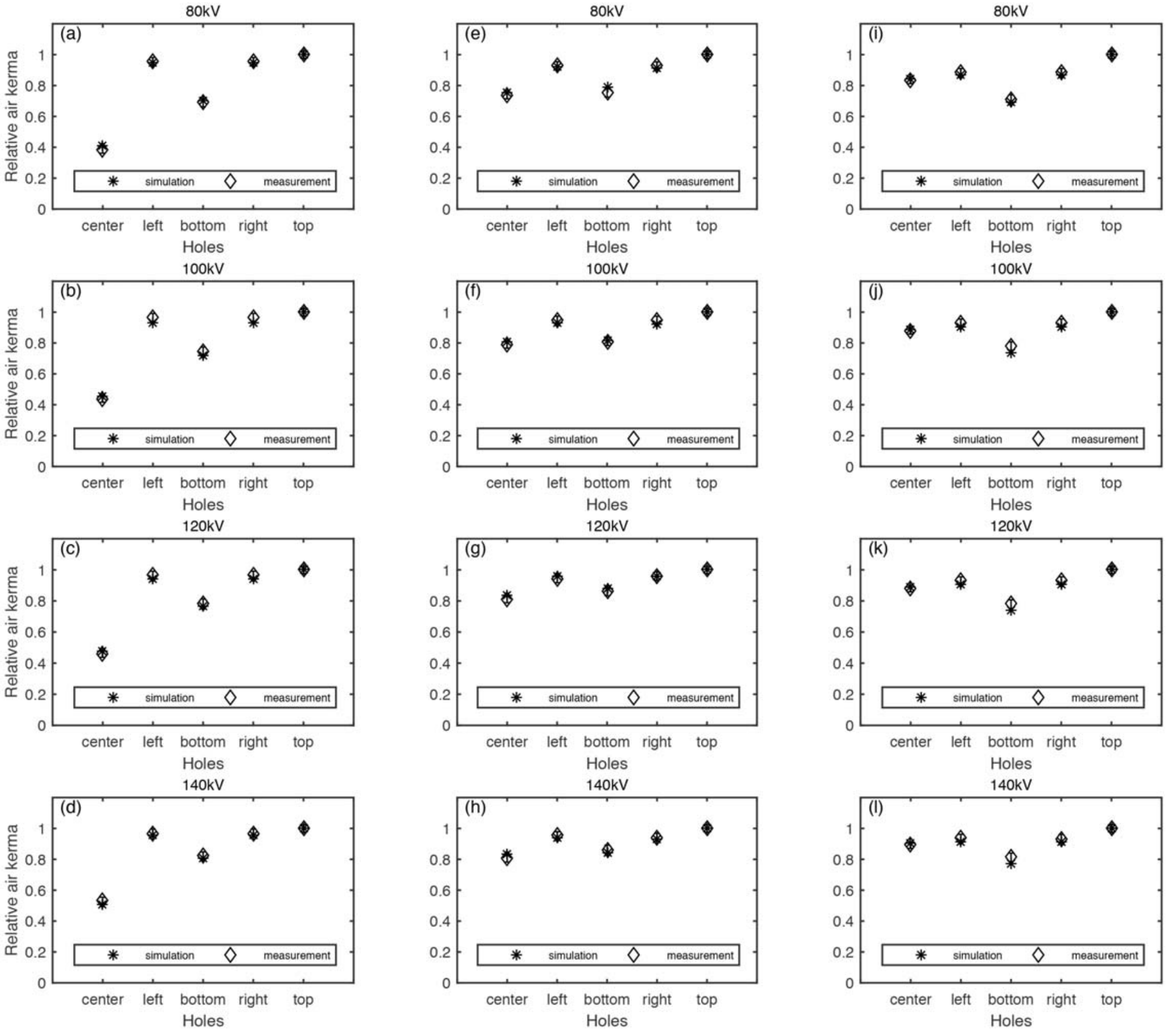
80kV
100kV
120kV
140kV
(a)
(b)
(c)
(d)
(e)
(f)
(g)
(h)
(i)
(j)
(k)
(l)
Relative air kerma
0
0.2
0.4
0.6
0.8
1
simulation
measurement
center
left
bottom
right
top
Holes